Published in final edited form as:

Xia, Y., Tian, Z., Heil, T., Meng, A., Cheng, B., Cao, S., et al. (2019). Highly selective CO_2 capture and its direct photochemical conversion on ordered 2D/1D heterojunctions. Joule, 3(11), 2792-2805. doi:10.1016/j.joule.2019.08.011.

Highly Selective CO_2 Capture and Its Direct Photochemical Conversion on Ordered 2D/1D Heterojunctions

Yang Xia, Zhihong Tian, Tobias Heil, Aiyun Meng, Bei Cheng, Shaowen Cao, Jiaguo Yu, Markus Antonietti

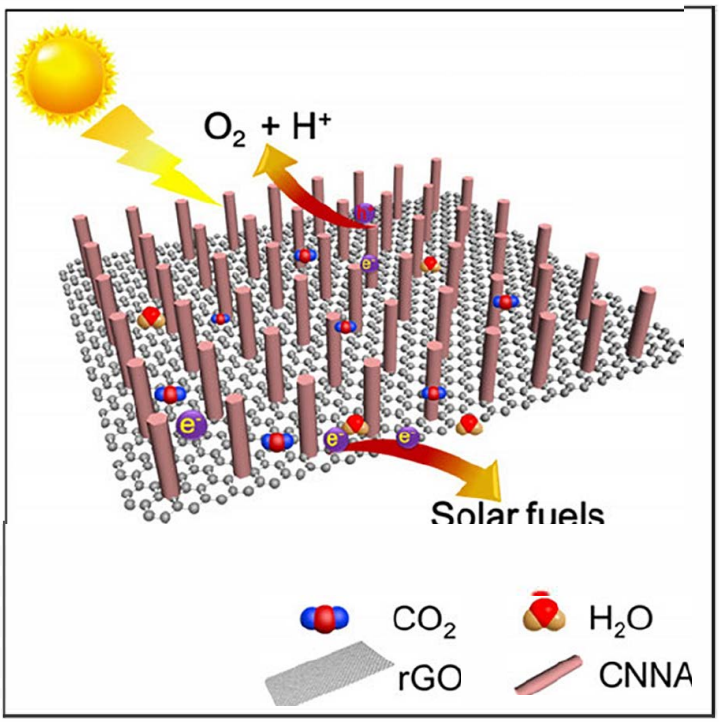

A heterojunction material involving highly crystalline carbon nitride nanorods with ordered alignment on graphene is successfully synthesized, and it shows a comparably high selectivity of CO_2/N_2 up to 44, with an isosteric heat of adsorption of 55.2 kJ/mol for CO_2. This material also shows remarkable improvements of light absorption, exciton splitting, and charge transport, which
enables the efficient photochemical reduction of wet CO_2 in the gas phase and without any sacrificial agent.

Highly Selective CO_2 Capture and Its Direct Photochemical Conversion on Ordered 2D/1D Heterojunctions

Yang Xia,[1] Zhihong Tian,[2] Tobias Heil,[2] Aiyun Meng,[1] Bei Cheng,[1] Shaowen Cao,[1,2,3,*] Jiaguo Yu,[1,*] and Markus Antonietti[2,*]

[1]State Key Laboratory of Advanced Technology for Materials Synthesis and Processing, Wuhan University of Technology, 430070 Wuhan, P. R. China

[2]Department of Colloid Chemistry, Max Planck Institute of Colloids and Interfaces, 14476 Potsdam, Germany

[3]Lead Contact

*Correspondence: swcao@whut.edu.cn (S.C.), jiaguoyu@yahoo.com (J.Y.), Markus.Antonietti@mpikg.mpg.de (M.A.)

SUMMARY

Polymeric carbon nitrides (CNs) are regarded as most sustainable materials for solar energy conversion via photocatalytic processes. However, the first-generation CNs suffered from imperfect charge separation and insufficient CO_2 adsorption. Herein, the construction of a heterojunction material involving highly crystalline CN-nanorods with ordered alignment on graphene is delineated, which improves light harvesting, CO_2 capture, and interface charge transfer. The graphene supported 1D nano-arrays of crystalline CNs shows a comparably high selectivity of CO_2/N_2 up to 44, with an isosteric heat of adsorption of 55.2 kJ/mol for CO_2. The heterojunction material also drives the simple and efficient CO_2 photoreduction in the gas phase, without the addition of any cocatalyst or sacrificial agent, even at the more relevant case of low concentrations of CO_2. These findings provide a robust way for tailoring the performance of carbon nitride materials, with the aim of a practicable technological application for CO_2 capture and photoreduction.

Keywords: CO_2 capture, CO_2 photoreduction, heterojunction, polymeric carbon nitride, graphene, charge transfer

INTRODUCTION

Artificial solar-driven CO_2 reduction into valuable fuels such as carbon monoxide (CO), methane (CH_4), and methanol (CH_3OH) based on semiconductor-mediated photocatalysis could be one of the long-term solutions to global warming and fuel shortage.[1-3] In many aspects, polymeric carbon nitrides (CNs) are the most promising candidates for CO_2 photoreduction among various semiconductor photocatalysts, because of their metal-free nature, low-cost and environmental friendly production, and appropriate electronic properties with sufficiently strong reduction by the photoelectrons in the conduction band.[4-7] However, the construction of an efficient and stable photochemical system for CO_2 reduction is still a challenge, because single-component semiconductors (including CNs) are less effective in exciton splitting towards single charge carriers, and the linear CO_2 molecules are chemically rather inert against activation during photocatalysis.[8-15] Hence, a second semi-conductor or semi-metal, for example, graphene, is necessary to form a bulk heterojunction which accelerates exciton splitting into the two subphases, charge transfer and surface catalytic processes then promoted by single charges. Graphene, the sp^2 bonded two-dimensional (2D) carbon material exhibits excellent conductivity and electron mobility and has a lower conduction band than carbon nitride, which helps to transfer and accumulate photoelectrons in the graphene subphase for

surface CO_2 reduction reaction,[16-19] while the carbon nitride then drives the oxidation reactions. At the same time, the improvement of CO_2 binding for a photocatalytic material is also of vital importance not only to improve the local CO_2 concentration, but also to improve the catalytic efficiency in surface CO_2 electron transfer reactions.

The first-generation of CNs, prepared by conventional thermal condensation of nitrogen-containing precursors still suffered from two weaknesses:[20-22] (1) low crystallinity with a larger content of defects, which is harmful for the bulk-to-surface charge migration of CNs; (2) tightly packed materials with low specific surface area, which largely reduce the interface contact area of CNs with the reaction media. To handle these aspects, we are trying to construct highly crystalline CN nanorods with an ordered alignment on graphene, in order to optimize the final performance of CO_2 photoreduction. Recently, it was shown that recondensation and recrystallization of melon in molten salts highly improves the structure of CNs, up to a practically fully condensed polyheptazineimide (PHI) structure with high crystallinity and reduced defects.[23-30] We expect that ordered nanostructures of highly crystalline CNs could be prepared with the assistance of suitable nucleation substrates.

In the current study, we describe the growth of one-dimensional (1D) nano-arrays of crystalline CN nanorods on graphene via an ionothermal

method. The ordered 1D crystalline structure provide channels for light harvesting and sufficient roughness to balance the (slow) oxidation reactions with the much faster reduction processes, and direct pathways for the transport of photoelectrons to the surface of graphene. The photo-absorption, bulk-to-surface and interface charge transfer of the resultant material are improved. Moreover, the unique 2D/1D heterojunction of graphene/CNs shows a (for covalent materials) high selectivity of CO_2/N_2 up to 44, with an isosteric heat of adsorption up to 55.2 kJ/mol for CO_2. As a consequence of these advantages, an excellent photocatalytic reduction of wet CO_2 into chemical fuels is acheived, in the gas phase and without any cocatalyst and sacrificial agent, even at a low concentration of CO_2.

RESULTS

Synthesis and Structural Analysis of 2D/1D Heterojunction of Graphene/CNs

The proof-of-concept experiments are illustrated in Scheme 1. At first melamine molecules were anchored via their amine groups onto the surface of graphene oxide (GO) through the C=O surface functionalities and hydrogen bridges. Under heating melamine was condensed to melon and grafted onto the graphene oxide, and the GO was reduced to gain the preheated melon/rGO hybrid. When this melon/rGO hybrid was

Scheme 1

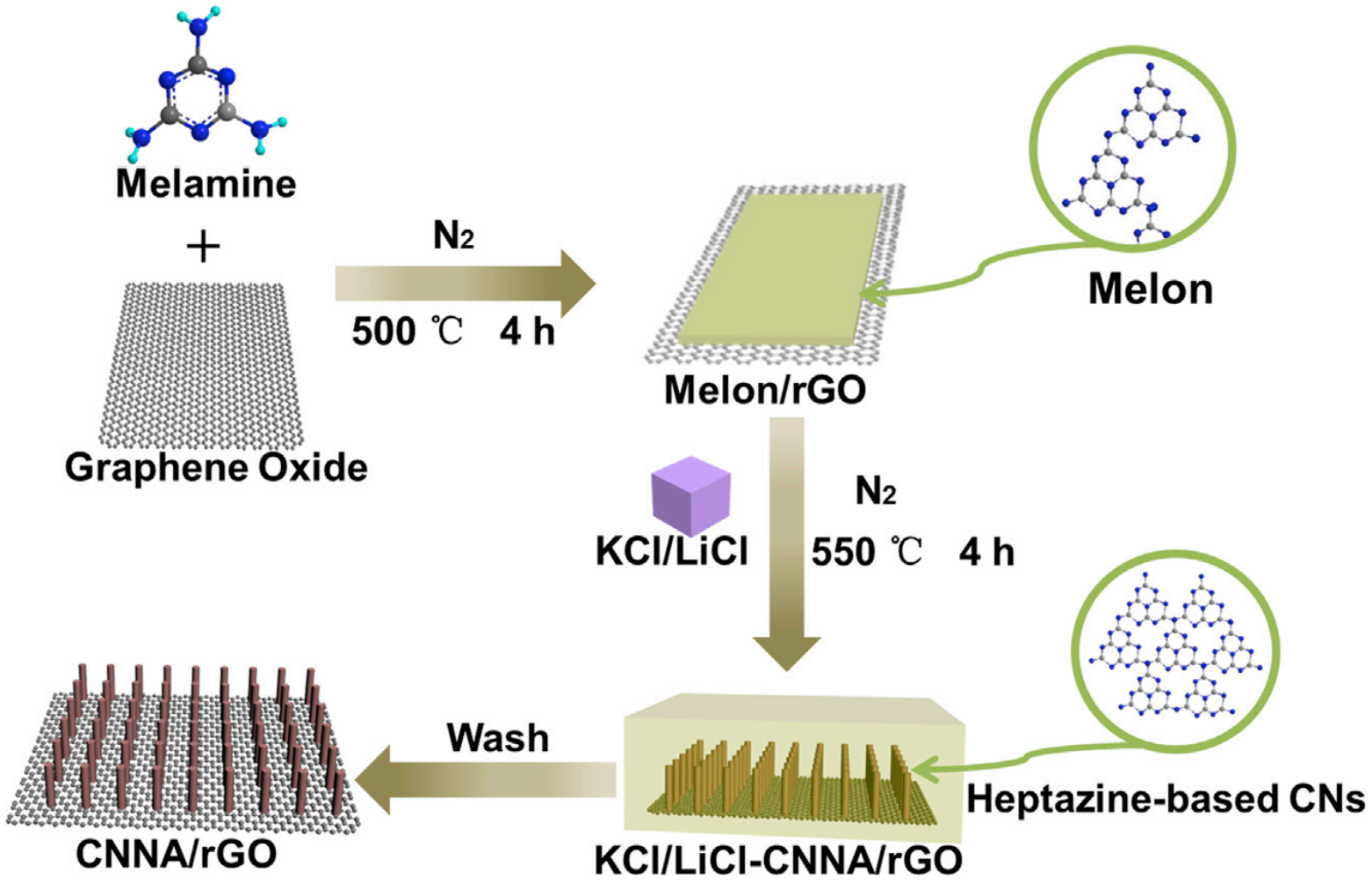

Scheme 1. Proof-of-Concept Experiments of 2D/1D Heterojunction of Graphene/CNs
The schematical formation of CNNA/rGO composite in the molten salt medium. rGO represents reduced graphene oxide.

dispersed in the molten salt (KCl/LiCl) flux at 550 °C, melon in partly solubilizes, recondenses and recrystallizes[31] from the graphene sheets to generate a vertically aligned morphology of PHI nanorods protruding from the graphene surface. Nucleation from graphene is potentially promoted by epitaxy, but also by the electronic interaction between the two precursor subphases.

As shown in Figure 1A, the powder X-ray diffraction (XRD) pattern of preheated carbon nitride (denoted as bCN) shows two characteristic diffraction peaks at 2θ = 13.0° (100) and 27.4° (200), which correspond to the repeated in-plane structural motif (0.68 nm) and the periodical interlayer-stacking (0.325 nm) of the aromatic rings, respectively.[32,33] The molten salt treatment leads to massive re-condensation of the conjugated framework and thus causes a downshift of (100) peak to 7.9° for the resultant polyheptazineimide (denoted as CNNA), showing a large intraplanar repeat period of 1.12 nm. Moreover, the sharper and narrower (002) peak of CNNA is located at 28.2°, indicating the formation of a highly crystalline CNs with a reduced interlayer distance of 0.316 nm. Note that the sample prepared in presence of graphene (denoted as CNNA/rGO) shows a similar XRD pattern to CNNA, suggesting that high crystallinity of CNs is not influenced by the accelerated nucleation of ordered nano-arrays from the graphene surface. The chemical structure of CN nanorods is also well retained despite the existence of graphene

Figure 1

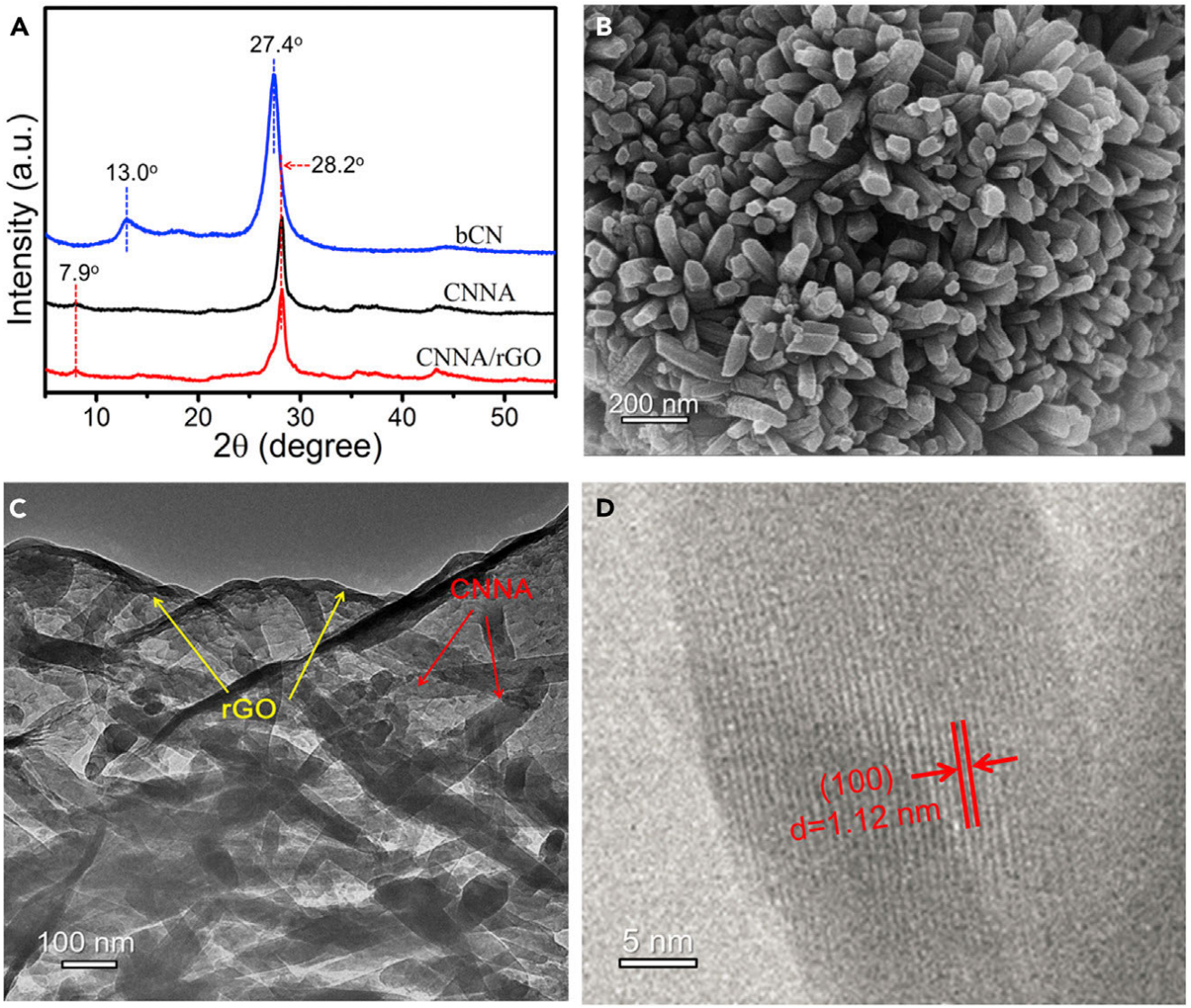

Figure 1. Characterization of 2D/1D Heterojunction of Graphene/CNs
(A) XRD patterns of the bCN, CNNA and CNNA/rGO. (B) FESEM and (C) TEM images of CNNA/rGO. (D) HRTEM image of the inner structure of a CN nanorod in CNNA/rGO.

as a growth substrate during the entire synthetic process, as evidenced by X-ray photoelectron spectroscopy (XPS) analysis. The survey spectra (Figure S1A) indicate the presence of C, N, O, K and trace-amount Cl^- on the surface of CNNA and CNNA/rGO. The high resolution XPS spectra of C 1s spectra (Figure S1B) show three peaks at 284.8 (potential surface impurities of sp^2 carbon, or graphene), 286.5 (C≡N/C-O), and 288.3 eV ($N=C-N_2$) for both CNNA and CNNA/rGO.[34-36] Meanwhile, the N 1s spectra (Figure S1C) indicate the existence of sp^2-hybridized nitrogen (398.7 eV), tertiary N groups (400.4 eV) and imide groups (401.3 eV) for both CNNA and CNNA/rGO, the weakest N 1s peak at 404.1 eV is due to the charging effects.[37-39] The K 2p spectra (Figure S1D) can be fitted into two small peaks at about 293.0 eV and 295.8 eV, which is in accordance with the binding energy of K^+ that coordinates to the electron-rich imide N atoms within the cavity of the PHI frameworks.[40] These integrated K^+ ions indeed help to delocalize the π electrons of nitrogen, thus facilitating the mobility and separation of photogenerated carriers.[41] The weak signals of Cl 2p at 197.8 and 199.6 eV (Figure S1E) indicate the tiny amount of Cl^- on the surface of CNNA and CNNA/rGO, which is likely entrapped in the structure during the crystallization process. No signal of Li 1s can be observed as shown in Figure S1F. In addition, the binding energies of the various elements for CNNA have been compared and contrasted with common poly (triazine

imide) (PTI) and polymeric CN materials from other literatures (Table S1), it was found that the Li^+ is easily incorporated into the common PTI, while the K^+ is easily incorporated into the CNNA.

The elemental analysis (EA, Table S2) indicates that the C/N molar ratio of CNNA is 0.73. This is close to the theoretical value of polymeric carbon nitride (0.75), suggesting the relatively higher structure order of CNNA as compared to weakly crystalline carbon nitride with more defects.[42] Note that the C/N molar ratio increases to 0.81 for CNNA/rGO, due to the good coupling of rGO with CNNA. Moreover, the atomic absorption spectroscopic analysis was used to detect the content of K, Li and Cl (Table S3). Only trace amount of Li and Cl was found in the samples, and the amount of K is 4.63 wt% and 3.82 wt% in CNNA and CNNA/rGO, respectively.

Fourier transform infrared (FTIR) spectra (Figure S2) reveal the existence of characteristic peaks of melon-based carbon nitride for both CNNA and CNNA/rGO. Especially, a new peak appeared at 1480 cm^{-1} in the spectrum of CNNA/rGO, which can be assigned to the skeletal vibration of the rGO sheets.[43] We have measured the solid-state ^{13}C and ^{15}N magic angle spinning (MAS) nuclear magnetic resonance (NMR) spectra, which are shown in Figure S3. In the ^{13}C NMR spectra (Figure S3A), two distinct peaks are observed at 156.7 and 163.5 ppm for bCN. The first resonance at δ_1 was related to the carbon atoms in "CN_3", and

the second resonance at δ_2 is attributed to the carbon atoms in "$CN_2(NH_x)$". Note that the spectra of CNNA and CNNA/rGO show three peaks. In addition to the two peaks at 156.7 and 163.5 ppm, a new peak appeared at 167.9 ppm (δ_3). This peak can be assigned to the carbon atoms in "$CH_2(N^-)$" due to the incorporation of potassium ions.[44] More importantly, in the ^{15}N NMR spectrum of CNNA/rGO (Figure S3B), the strong isolated signal at 230.5 ppm can be identified to the central nitrogen atom (Nc) in the heptazine core, suggesting the heptazine-based nature of CNNA. The signals between 160 and 200 ppm are characteristic of tertiary nitrogen atoms (N_{tert}). The signals between 250 and 265 ppm are assigned to NH groups, and the remaining signals at 269, 274 and 281 ppm belong to NH_2 groups. These results (especially the ^{15}N NMR spectrum) confirm the presence of heptazine units in CNNA/rGO.[45-47]

SEM images show that bCN (Figure S4A) is severely aggregated and rather densely packed, while CNNA (Figure S4B) is composed of randomly distributed nanorods. In contrast, CNNA/rGO (Figure 1B and S4C) exhibits a regular composite structure with a vertical alignment of nanorods to the graphene nucleation planes. A typical length of around 200–400 nm and diameter of about 15–40 nm can be taken from SEM and the TEM images (Figure 1C and S4D). TEM also confirms that the CN nanorods are tightly anchored at the surface of graphene. The

elemental mapping (Figure S5) of the CNNA/rGO clearly shows the homogenous distribution of the elements C, N and O. The HRTEM observation (Figure 1D) of a single CN nanorod further demonstrates the high crystallinity with organized lattice fringes of 1.12 nm parallel to the long axis, i.e. the nanorods grow into the z-direction, the direction of charge transport, with all the catalytically active edge sites exposed to the outer medium. The crystallization and microstructure evolution caused by molten salt treatment has led to a remarkably increased specific surface area from 7 m^2 g^{-1} (for bCN) to 64 m^2 g^{-1} (for CNNA) (See Table S4 and Figure S6). Note that CNNA/rGO shows both slightly reduced specific surface area (55 m^2 g^{-1}) and interstitial nanorod-mesopores.

Optical and Charge Transfer Properties of 2D/1D Heterojunction of Graphene/CNs

The optical properties shown in Figure 2A reveal a red shift of absorption edge from 460 nm (for bCN) to 475 nm (for CNNA), corresponding to a slight band gap narrowing from 2.70 eV to 2.61 eV. This is typical for PHI-K materials and related to the improved interlayer packing.[48] Moreover, CNNA exhibits a significantly higher extinction coefficient, typical for nanopigments of strongly absorbing materials where colour strength depends on particle size. The introduction of rGO further

Figure 2

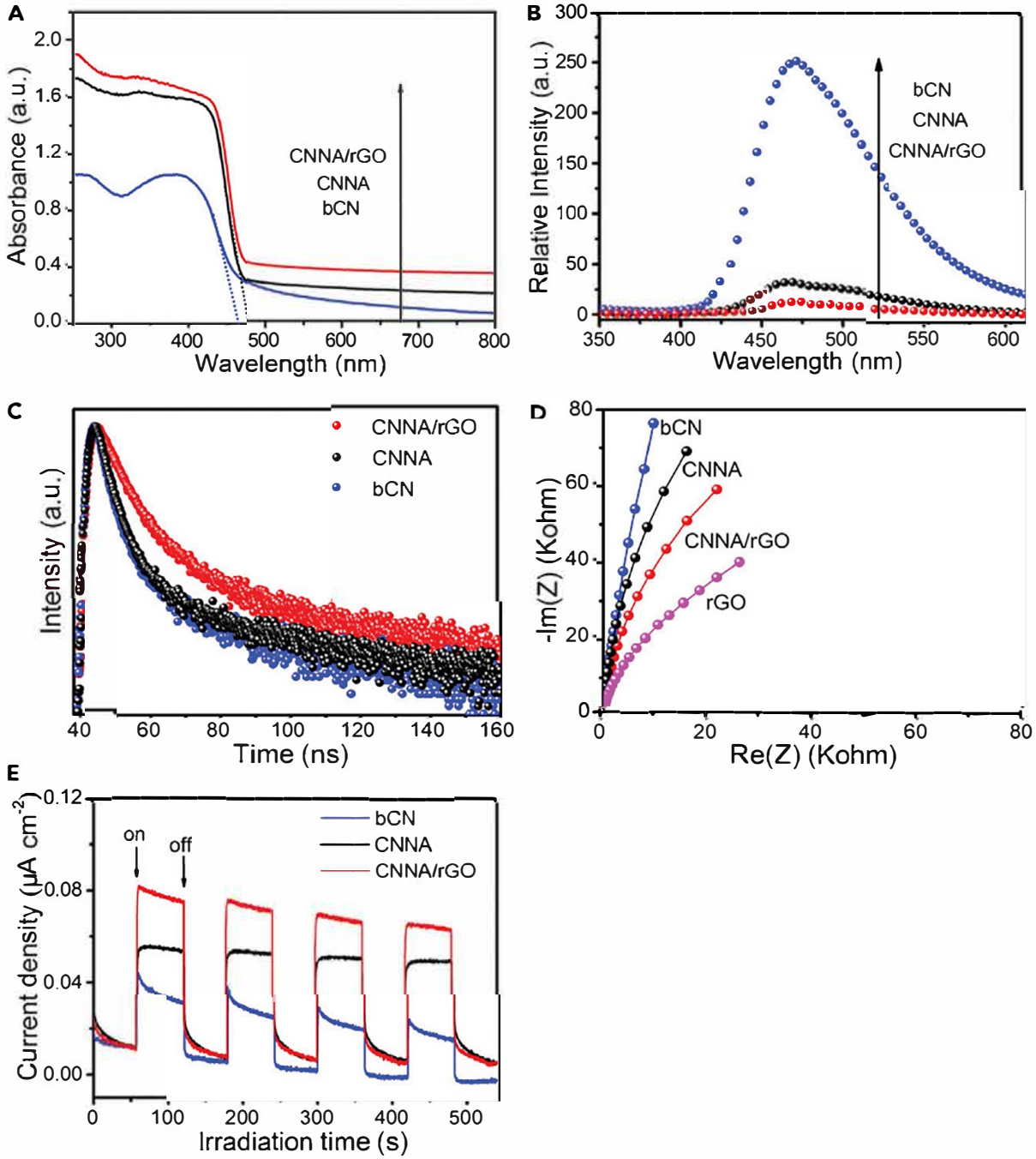

Figure 2. Optical and Charge Transfer Properties of 2D/1D Heterojunction of Graphene/CNs
(A) UV - vis diffuse reflectance spectra (DRS),
(B) steady−state room−temperature PL spectra,
(C) TRPL spectra of bCN, CNNA, and CNNA/rGO,
(D) EIS Nyquist plots of bCN, CNNA, rGO and CNNA/rGO, and
(E) transient photocurrent responses of bCN, CNNA and CNNA/rGO.

enhances the photo-absorption in the range of <450 nm and 450–800 nm, which we attribute to charge transfer and the formation of an active heterojunction, bringing relaxation strength. This adds to the weak background absorption of carbon.

The nanostructure and the well operative heterojunction improve exciton splitting and charge transfer, as also seen by the remarkably decreased emission intensity of CNNA photoluminescence (PL) (Figure 2B). Improved crystallinity already helps charge transport to the surface, but the lowest PL intensity is found for CNNA/rGO. The time-resolved transient photoluminescence (TRPL) analysis (Figure 2C) gives an average fluorescence lifetime (τ_A) of 7.18, 8.82 and 12.58 ns for bCN, CNNA and CNNA/rGO (see Table S5), demonstrating indeed the lowering of defects and grain boundaries which act as internal recombination sites. Moreover, after the introduction of rGO, the interfacial charge transfer is improved. Hence, charges have to travel longer until they are much more rarely recombined due to synergistic effect of high crystallinity of CN nanorods and heterojunction effect of CNNA/rGO.[49,50] The improvement of solid state conductivity is further confirmed by electrochemical impedance spectroscopy (EIS) where smaller radius is found in Nyquist plots (Figure 2D) of CNNA/rGO in comparison with bCN and CNNA. rGO has the smallest radius, indicating its good conductivity and demonstrating that rGO contributes to the low resistance or high electron mobility of CNNA/rGO. In addition, we find the largest photocurrent (Figure 2E)

in a CNNA/rGO-based electrode, indicating again the low degree of charge recombination and the low charge-transfer resistance of CNNA/rGO. For bCN, a photocurrent spike appeared and then a slow reduction in photocurrent was observed when the working electrode was under light irradiation. This was mainly due to the rapid recombination of photogenerated electrons and holes and subsequently, the photocurrent dropped steeply as the light switched off. In contrast, for CNNA, the photocurrent kept relatively stable when the light switched on. This was because the lower defect density enabled the photogenerated electrons to transfer to the cathode with lower recombination rate. After light off, those electrons would travel longer distance, i.e., longer decay time. The photocurrent curve of CNNA/rGO displayed similar shape with the CNNA. In addition to effective charge migration across CNNA, rGO helped to accumulate these separated electrons, which gradually decayed after switching off the light.[51-53]

CO_2 Capture Performance of 2D/1D Heterojunction of Graphene/CNs

The CO_2 adsorption performance of the materials at different temperature is shown in Figure S7. At 298K, CNNA and CNNA/rGO show similar CO_2 adsorption capacity, but it is much higher than that of bCN, CN/rGO-Li and CN/rGO-K. SEM observation in Figure S8 suggests that CN/rGO-Li and CN/rGO-K are composed of bulk solid agglomerates and cannot form the nanorod arrays. These results indicate that the main

Figure 3

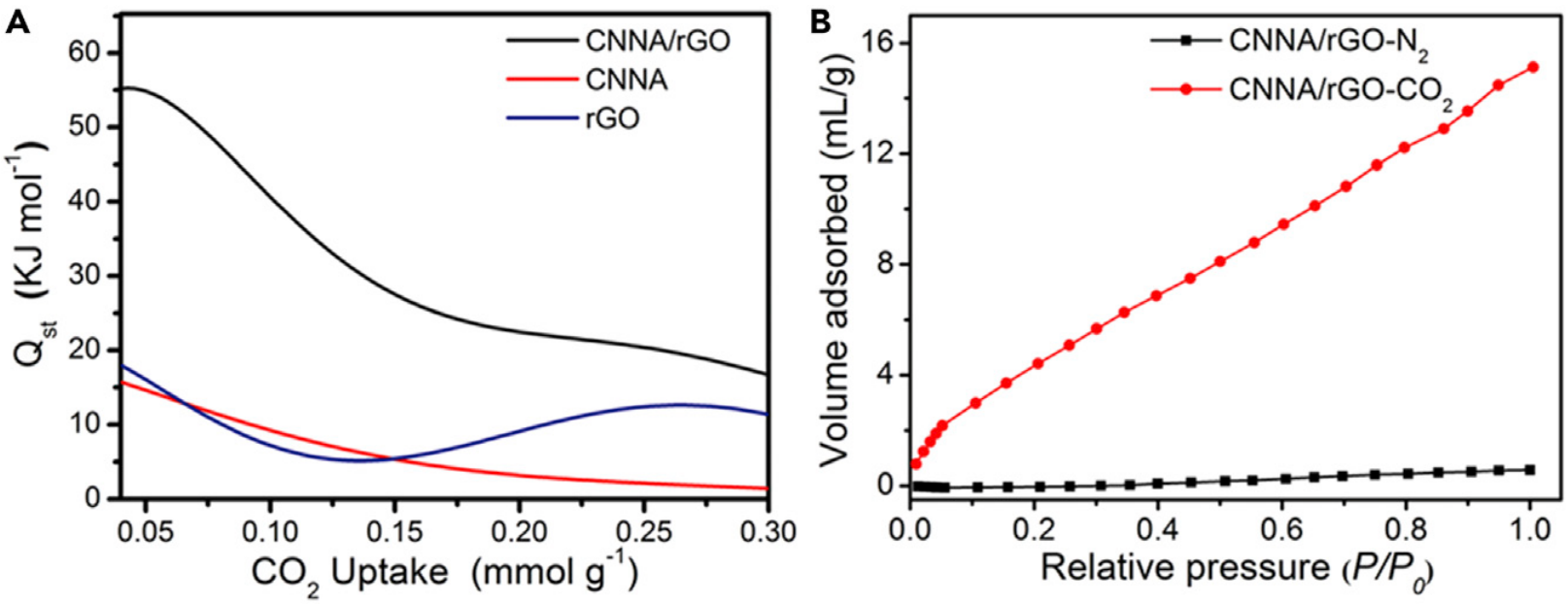

Figure 3. CO_2 Adsorption of 2D/1D Heterojunction of Graphene/CNs
(A) The calculated isosteric heat (Qst) of CO_2 adsorption on CNNA, rGO and CNNA/rGO. (B) Adsorption isotherms of CO_2 and N_2 on CNNA/rGO at 273K and 1 atm.

reason of the improved CO_2 adsorption performance are the heterojunction effect and ordered 1D structure rather than K incorporation. More importantly, CNNA/rGO shows a remarkably higher temperature dependence of CO_2 adsorption capacity than CNNA, bCN and rGO. This result reveals a much stronger adsorption strength between CO_2 molecules and the surface of CNNA/rGO, which could be further quantified by calculating the isosteric heat (Q_{st}) of CO_2 adsorption using the Clausius–Clapeyron equation.[54] As shown in Figure 3A, the low-coverage isosteric heat of CO_2 adsorption calculated for CNNA/rGO could be up to 55.2 kJ/mol, which is much higher than that for CNNA (15.7 kJ/mol) and rGO (18.2 kJ/mol). This value is even higher than many reported values for specialized CO_2 capture materials such as porous carbon materials,[55,56] porous polymer networks[57,58] and MOF materials,[59,60] indicating an unusually strong chemisorption of CO_2 molecules onto the surface of CNNA/rGO. The high Q_{st} of CNNA/rGO clearly underlines the heterojunction effect already when not illuminated. Charge transfer from rGO to CNNA changes the electronic environment and causes charge redistribution, obviously improving polarity and polarizability and thereby the adsorption strength.[61,62] As shown in Figure 3B, the CO_2 uptake increases sharply as the pressure increases, while the N_2 adsorption capacity only slightly increases in the pressure range. The calulated CO_2/N_2 selectivity is 44, which is even comparable to

those values of performance separation products. The Q_{st} decreases monotonically with the surface coverage by the restrictions of heterojunction charge transfer, which is less than monolayer coverage, i.e. just the first CO_2 molecules can be activated in that mode. These CO_2 adsorption motifs are ideally set for photocatalytic materials, because photoelectrons have a direct transfer path to the strongly bound CO_2 molecules, while the less polarizable reaction products get released from the surface. As compared to typical CO_2 adsorption materials, the adsorption capacity values looks low, but we must consider that the samples as functional photocatalysts are not porous, i.e. they have only 2.5 % of the specific interface to compare with. In terms of adsorption per contact area, the values are indeed remarkably high and already set in at rather low relative pressures. In this case, a strongly polarizing surface is more important for CO_2 uptake at 1 bar than a high specific surface area, as accessed by nitrogen sorption.[62]

Photocatalytic CO_2 Reduction Activity of 2D/1D Heterojunction of Graphene/CNs

The as-prepared materials were applied in one of the most demanding reactions of artificial photosynthesis, the photocatalytic gas-phase CO_2 reduction, in the absence of any sacrificial agent. Note that for closing the redox cycle the CO_2 must be wet, i.e. the reaction is:

Figure 4

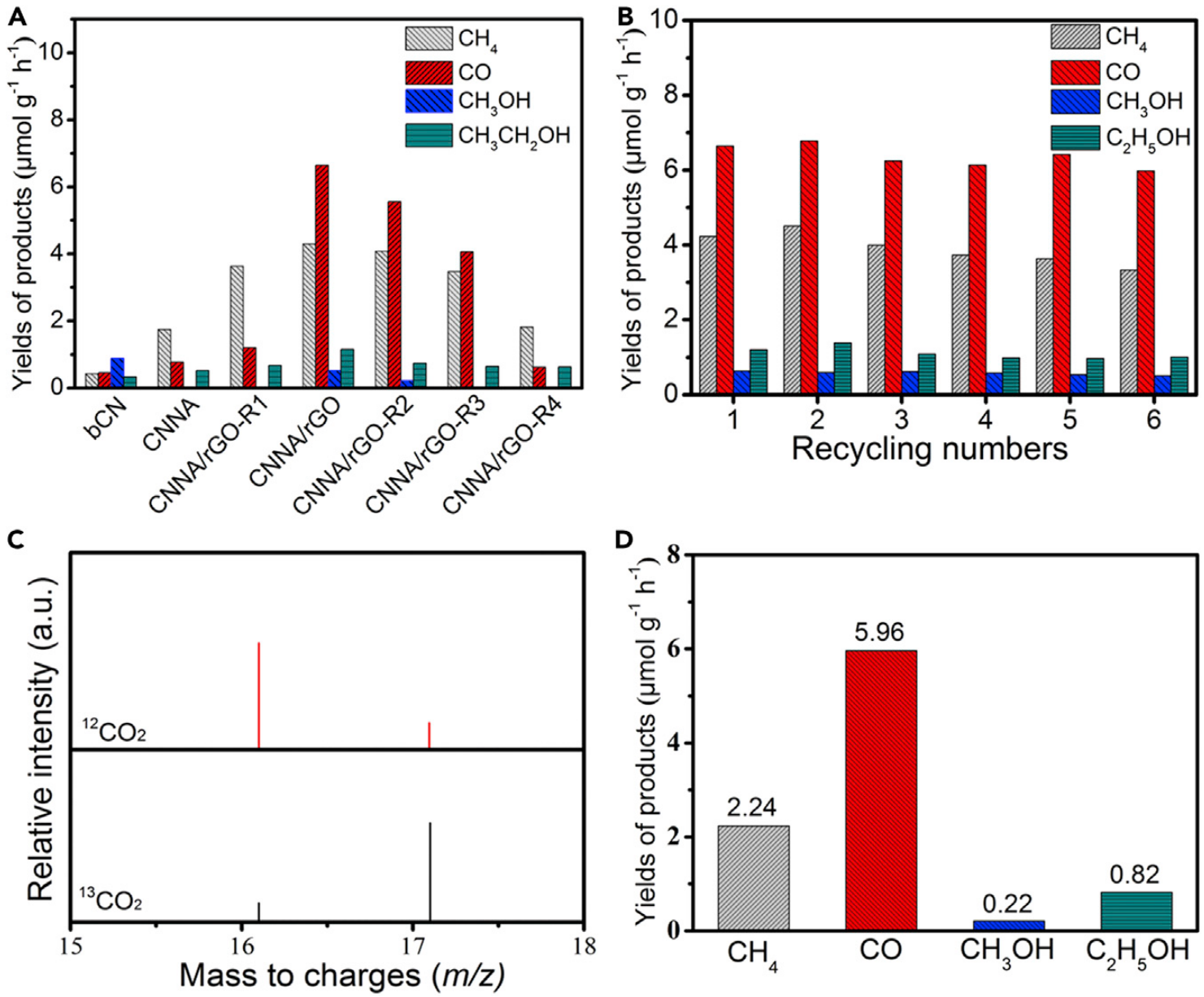

Figure 4. CO_2 Photoreduction Properties of 2D/1D Heterojunction of Graphene/CNs
(A) Photocatalytic CO_2−reduction property of bCN, CNNA, CNNA/rGO−R4 and CNNA/rGO at various amount of rGO in water vapor−saturated wet CO_2 gas. (B) Cycling test of photocatalytic CO_2 reduction over CNNA/rGO. (C) GC−MS analysis of methane labeled by 13C and 12C from photocatalytic CO2−reduction reactions over CNNA/rGO. (D) Photocatalytic CO2−reduction property of CNNA/rGO in low−concentration CO_2 gas phase.

$$CO_2 + H^+ + e^- \rightarrow C_xH_yO_z + H_2O \qquad (1)$$

$$H_2O + h^+ \rightarrow O_2 + H^+ \qquad (2)$$

First, a reaction environment of water vapor-saturated wet CO_2 gas was employed. Control experiments confirmed that no noticeable product was observed in the absence of photocatalyst, CO_2 or light irradiation, which also excludes bare decomposition of the catalyst as a source of chemical compounds. For the real reaction, indeed a spectrum of fuel molecules is found. Figure 4A and Table S6 shows the yield of these main products of CO_2 reduction, i.e. C=O, CH_4, CH_3OH, and C_2H_5OH over various photocatalysts. CNNA exhibits better CO_2 photoreduction performance than the reference bCN, but the binary CNNA/rGO shows the best performance with a total CO_2 conversion of 12.63 μmol h^{-1} g^{-1}. This value can be compared with other optimized systems of carbon nitride-based photocatalysts (Table S7) as well as graphene-based photocatalysts (Table S8) for CO_2 reduction and turned out to be comparably high. Note that CNNA with higher crystallinity is beneficial for the formation of C_2H_5OH in comparison with CH_3OH. The introduction of rGO further increases the production rate of C_2H_5OH noticeably, possibly because rGO helped to accumulate the photoelectrons and improve the CO_2 adsorption. C_2H_5OH can be produced by coupling of methoxyl ($\bullet OCH_3$) and methyl ($\bullet CH_3$) radicals, which served as reaction intermediates during the process of

photocatalytic CO_2 conversion.[63,64] Additionally, in order to investigate the effect of trace-amount metal on photocatalytic performance, reference samples of bCN-K and bCN+K (4.6 wt% KCl was ground with bCN) were prepared for photocatalytic CO_2 reduction and the products are shown in Table S6. It is noted that CH_4, CO, CH_3OH, C_2H_5OH and H_2 yields for bCN+KCl has little change as compared to those of bCN. While CH_4, CO, CH_3OH, C_2H_5OH and H_2 yields for bCN-K are increased, which is because the doped K could act the electron donor and facilitate the electron transfer between the layers of bCN.[38,41] The total quantum yield of CO_2 conversion into CH_4, CO, CH_3OH, and C_2H_5OH was measured as 0.254 % under 420-nm light irradiation (see also Table S9). The turnover number (TON) of CNNA/rGO for photocatalytic CO_2 reduction is 1.6, under simulated solar light irradiation with 4 hours. Moreover, only a minor amount of H_2 could be detected over CNNA/rGO (1.93 μmol h^{-1} g^{-1}). Importantly, the yield of H_2 is much lower than the conversion of CO_2, which demonstrates the high selectivity of CO_2 photoreduction (87%) in this cocatalyst-free and sacrificial agent-free system, with reference to hydrogen evolution that is otherwise the competing side reaction. We also checked for the oxidation product and found dioxygen, accordingly (Figure S9), which is the product of water oxidation for the closure of the photoredox cycle. We have calculated the detected yield of O_2 from photocatalytic CO_2 reduction on CNNA/rGO, which is 21.15

μmol g^{-1} h^{-1}. Given that the water oxidation to O_2 is the sole reaction to consume the photogenerated holes ($2H_2O = O_2 + 4H^+ + 4e^-$), CO_2 is reduced by accepting H^+ and e^- to form CO, CH_4, CH_3OH and C_2H_5OH. Thus, the stoichiometric yield of O_2 should be calculated as 17.14 μmol g^{-1} h^{-1}, which is slightly lower than the detected yield. Such deviation is reasonable within experimental errors and might be related to the undetectable species beyond the GC limitation. Ultraviolet photoelectron spectroscopic (UPS) measurements in Figure S10A show that the valence band energies of CNNA and CNNA/rGO are calculated to be 1.25, and 1.36 V, respectively (vs. NHE, pH=7), which are located much more positively than the oxidation level (0.82 V) for H_2O to O_2, allowing holes to transfer and react with H_2O molecules (see diagram in Figure S10B). Meanwhile, it also reveals that the presence of rGO in CNNA/rGO can obviously adjust the band structure of CNNA. This is analogous to the previous studies on GO/reduced blue titania and black phosphorus/CN.[65,66] Furthermore, after the introduction of rGO, the high crystallinity of CNNA and good conductivity of rGO promote the charge migration and separation at the surface/interface. The electrons accumulate on the surface of rGO and subsequently reduce CO_2, leaving behind the holes in carbon nitride to oxidize water (see Figure S11). Note that inadequate or excessive loading of rGO causes a lowered CO_2 photoreduciton efficiency (See data of CNNA/rGO-R1, R2

and R3 in Figure 4A and Table S6), i.e. it is important to match the reduction and oxidation sites in a system engineering approach.[67] With increasing loading amount of rGO in CNNA, the composites have different light absorption properties, resulting in the difference in the light intensity profile through the photocatalytic system, while these changes are nonlinear with respect to mass fractional composition. Therefore, non-synergistic activity at higher loading amount of rGO correlates nonlinearly with mass fractional composition of rGO.[68] Another reference sample with grinding (CNNA/rGO-R4, see experimental details in Supplemental information) shows much lower product yields than that of CNNA-rGO sample, demonstrating the importance of the first organization between melamine and GO. The excellent photocatalytic stability of CNNA/rGO was demonstrated by a 9-h cycling test, as shown in Figure 4B. In addition, the XRD and XPS of CNNA/rGO were measured after the 9-h cycling test and showed no obvious change (Figure S12 and S13).

To confirm the carbon source of the photocatalytic products is CO_2, gas chromatography–mass spectrometry (GC-MS) was used to detect $^{12}CH_4$ and $^{13}CH_4$ in the presence of isotope labelled CO_2. As shown in Figure 4C, it is obvious that the peak of m/z = 16.1 ($^{12}CH_4$) and m/z = 17.1 ($^{13}CH_4$) were dominated in the GC–MS spectra of photocatalytic ^{12}C-labeled CO_2 and ^{13}C-labeled CO_2 reduction, respectively. The weak

signal at m/z=16 when using $^{13}CO_2$ as the carbon source belongs to $^{13}CH_3$ due to the ionization.[69,70] The isotopic labelling experiments about the carbon and hydrogen sources labeled by ^{13}C, ^{12}C and ^{2}H (D) from photocatalytic CO_2-reduction reactions over CNNA/rGO were also performed and the results are displayed in Figure S14. The signals of molecular ions for alcohol are at m/z = 45.1, m/z = 47.1 and m/z = 51.1 when using $^{12}CO_2$ to react with H_2O (Figure S14A), $^{13}CO_2$ to react with H_2O (Figure S14B) and $^{12}CO_2$ to react with D_2O (Figure S14C), respectively. Note that the intensity of the peaks at m/z =45.1, m/z = 47.1 and m/z = 51.1 is stronger than that of the peak at m/z = 46.1 ($^{12}C_2H_5OH$), m/z = 48.1 ($^{13}C_2H_5OH$) and m/z = 52.1 (C_2D_5OD) due to the higher stability of molecular ions. These results strongly support that the photocatalytic products originate from CO_2 reduction.

Then, an experiment with lower concentration of CO_2 and high concentration of N_2 (similar to flue gas) was employed. As compared to the above-mentioned condition of wet CO_2 gas, nearly 90 vol.% of CO_2 was replaced by N_2. It is surprising that the CNNA/rGO heterojunction material still exhibits a relatively good activity (see Figure 4D), and the total CO_2 conversion could still be as high as 9.24 μmol h^{-1} g^{-1}, demonstrating the benefits originating from the unique CO_2 adsorption behavior with high selectivity and strong binding affinity.

DISCUSSION

The simple synthesis of a uniquely structured and highly active photocatalyst has been presented. Nano-arrays of crystalline carbon nitride rods are grown on rGO. The obtained hybrid material with regular and crystalline microstructure operates as a colloidal heterojunction and shows remarkable improvements of light absorption, exciton splitting, charge transport, as well as selective CO_2 binding, which enables the highly efficient photochemical reduction of wet CO_2 into chemical fuels, here in the gas phase and without any sacrificial agent. This occurs even at the more relevant case of CO_2 concentrations similar to flue gas. This finding represents to our opinion a relevant strategy of structure design of polymeric carbon nitride hybrids toward a potential technological application of CO_2 capture and photoreduction. Following work will consider to work on the system engineering approach to further improve activity, as well as to handle educt enrichment and product release.

EXPERIMENTAL PROCEDURES

Sample preparation

Graphene oxide was synthesized from the natural graphite powder by modified Hummers method.[71] The carbon nitride nanorod arrays supported on rGO (CNNA/rGO) was prepared by an ionothermal method. Typically, 3 g of melamine powder and 3 mL of GO aqueous solution (1.0

g/L) were added into 50 mL deionized water under vigorous stirring. The formed suspension was dried at 80 °C overnight and then calcined at 500 °C for 4 h with a heating rate of 10 °C/min under N_2 atmosphere. After cooling to room temperature, the preheated bCN/rGO was obtained. Thereafter, 0.5 g of preheated sample was mixed with KCl (2.75 g) and LiCl (2.25 g), and ground on the hot plate at 100 °C. After that, the mixture was heated in N_2 atmosphere at a heating rate of 5 °C/min to 550 °C for 4 h. The final product was washed with boiling distilled water, and then followed by drying at 60 °C overnight in a vacuum oven. Reference samples of CNNA/rGO-R1, R2 and R3 were prepared using the similar procedure, except that the volume of GO aqueous solution was 1 mL, 5 mL and 7 mL. Reference samples of CNNA, CN/rGO-Li, CN/rGO-K were prepared by the same procedure without adding graphene oxide, KCl, and LiCl respectively. The preheated carbon nitride without adding graphene oxide before molten salt treatment was labeled as "bCN". The reference sample of CNNA/rGO-R4 was also prepared, by grinding the preheated carbon nitride with GO and subsequent treatment of molten salt (see experimental details in Supplemental information). The reference sample of bCN-K was prepared by the same procedure of bCN, but with the addition of KCl (see experimental details in Supplemental information).

CO_2 and N_2 adsorption measurements

CO_2 adsorption measurements were carried out up to 1 bar at 273 K (ice-water bath) and 298 K (room temperature) on a Quantachrome Quadrasorb SI apparatus. Before adsorption, the samples were degassed at 200 ˚C under vacuum for 12 h. The same test procedure was adapted for the N_2 adsorption measurements at 273 K.

The selectivity (S_{IAST}) for binary gas mixtures of CO_2 and N_2 is calculated based on the Ideal Adsorption Solution Theory (IAST) and is defined as:

$$S_{IAST} = \frac{q_{CO_2}/q_{N_2}}{p_{CO_2}/p_{N_2}} \quad (3)$$

Where q_{CO_2} and q_{N_2} are the molar loading of CO_2 and N_2, mmol g^{-1}; P_{CO_2} and P_{N_2} are the partial pressure of CO_2 and N_2, respectively.

Photocatalytic CO_2 reduction in water vapor-saturated wet CO_2 gas

The photocatalytic performance of the samples was evaluated by CO_2 photoreduction in a 200 mL customized Pyrex reactor with two necks. Particularly, 100 mg of sample was added to the reactor, dispersed in 10 mL deionized water by ultrasonication, and then dried at 80 ºC to form a smooth and thin film on the bottom of the reactor. The wet CO_2 was blown through the reactor for 30 min to ensure anaerobic conditions of the reaction system, and used as CO_2 and H_2O sources. A 350 W Xe arc lamp with an AM1.5 filter was employed as simulated sunlight source to irradiate the reactor. The resulting gas species were monitored and recorded by a gas chromatography with a FID and a TCD detector, and a

methanizer (PGC-80, PANNA, CHINA). The standard curves of CH_4, CO, CH_3OH and C_2H_5OH were recorded by using commercial standard gases.

Photocatalytic CO_2 reduction in low-concentration CO_2 gas

Similar to the above procedure, the photocatalyst (100 mg) was put onto the bottom of a two-neck Pyrex reactor (200 mL) with two parallel planes. Next, $NaHCO_3$ (0.084 g) was carefully put into a groove on one of the necks. Then the two necks were sealed with the rubber plugs. After that, this reactor was purged with nitrogen for 1 h. The CO_2 gas was generated from a simple reaction between H_2SO_4 and $NaHCO_3$ in the sealed reactor. Particularly, 0.3 mL of 2 M H_2SO_4 was elaborately injected into the groove to react with $NaHCO_3$. A 350 W Xe arc lamp with an AM1.5 filter was employed as simulated sunlight source to irradiate the reactor. The resulting gas species were monitored and recorded by a gas chromatography with a FID and a TCD detector, and a methanizer (PGC-80, PANNA, CHINA).

Isotopic measurement

The experimental process of isotopic measurement is same with that of photocatalytic CO_2-reduction experiments, except that the $NaH(^{12}C)O_3$ is replaced by the $NaH(^{13}C)O_3$ (Cambridge Isotope Laboratories Inc., USA) and the H_2O is replaced by the D_2O (Cambridge Isotope Laboratories Inc., USA). Then, the $^{12}CH_4$, $^{13}CH_4$, $^{12}C_2H_5OH$, $^{13}C_2H_5OH$ and C_2D_5OD

species were detected by a gas chromatography-mass spectrometer (Agilent Technologies 6890N GC system with 5975 MSD, USA).

SUPPLEMENTAL INFORMATION

Supplemental Information includes characterizations, photoelectrochemical measurement, 14 figures, and 9 tables and can be found with this article online at https://doi.org/10.1016/j.joule.xxxxxx.

ACKNOWLEDGMENTS

The authors acknowledge the financial support from the National Natural Science Foundation of China (21773179, U1705251 and 21433007) and Max Planck Society, and the Natural Science Foundation of Hubei Province of China (2015CFA001 and 2017CFA031).

AUTHOR CONTRIBUTIONS

M.A., J.Y., S.C. and Y.X. conceived and designed the experiments. Y.X. carried out the synthesis of the materials and photocatalytic test. Z.T. performed the CO_2 adsorption test. Y.X., Z.T., T.H., A.M. and B.C. performed materials characterizations. Y.X., Z.T., T.H., A.M., B.C. and S.C. contributed to data analysis. M.A., J.Y. and S.C. supervised the project. M.A., J.Y., S.C. and Y.X. wrote the paper. All authors discussed the results and commented on the manuscript.

DECLARATION OF INTERESTS

The authors declare no competing interests.

REFERENCES

1. Liu, X., Inagaki, S., and Gong, J.L. (2016). Heterogeneous Molecular Systems for Photocatalytic CO_2 Reduction with Water Oxidation. Angew. Chem. Int. Ed. *55,* 14924-14950.
2. Ran, J.R., Jaroniec, M., and Qiao, S.Z. (2018). Cocatalysts in Semiconductor-based Photocatalytic CO_2 Reduction: Achievements, Challenges, and Opportunities. Adv. Mater. *30,* 1704649.
3. Bushuyev, O.S., De Luna, P., Dinh, C.T., Tao, L., Saur, G., van de Lagemaat, J., Kelley, S.O., and Sargent, E.H. (2018). What Should We Make with CO_2 and How Can We Make It? Joule *2,* 825-832.
4. Ong, W. J., Tan, L.L., Ng, Y. H., Yong, S.T., and Chai, S.P. (2016). Graphitic Carbon Nitride (g-C_3N_4)-Based Photocatalysts for Artificial Photosynthesis and Environmental Remediation: Are We a Step Closer To Achieving Sustainability? Chem. Rev. *116,* 7159-7329.
5. Fang, Y. X., and Wang, X.C. (2018). Photocatalytic CO_2 Conversion by Polymeric Carbon Nitrides. Chem. Commun. *54,* 5674-5687.

6. Cao, S.W., Low, J.X., Yu, J.G., and Jaroniec, M. (2015). Polymeric Photocatalysts Based on Graphitic Carbon Nitride. Adv. Mater. *27,* 2150-2176.

7. Kessler, F. K., Zheng, Y., Schwarz, D., Merschjann, C., Schnick, W., Wang, X.C., and Bojdys, M.J. (2017). Functional Carbon Nitride Materials Design Strategies for Electrochemical Devices. Nat. Rev. Mater. *2,* 17030.

8. Cometto, C., Kuriki, R., Chen, L.J., Maeda, K., Lau, T.C., Ishitani, O., and Robert, M. (2018). A Carbon Nitride/Fe Quaterpyridine Catalytic System for Photostimulated CO_2-to-CO Conversion with Visible Light. J. Am. Chem. Soc. *140,* 7437-7440.

9. Liang, L., Li, X., Sun, Y., Tan, Y., Jiao, X., Ju, H., Qi, Z., Zhu, J., and Xie, Y. (2018). Infrared Light-Driven CO_2 Overall Splitting at Room Temperature. Joule *2,* 1004-1016.

10. Kuehnel, M.F., Orchard, K.L., Dalle, K.E., and Reisner, E. (2017). Selective Photocatalytic CO_2 Reduction in Water through Anchoring of a Molecular Ni Catalyst on CdS Nanocrystals. J. Am. Chem. Soc. *139,* 7217-7223.

11. Wang, L., Ghoussoub, M., Wang, H., Shao, Y., Sun, W., Tountas, A.A., Wood, T.E., Li, H., Loh, J.Y.Y., Dong, Y., *et al.* (2018). Photocatalytic Hydrogenation of Carbon Dioxide with High Selectivity to Methanol at Atmospheric Pressure. Joule *2,* 1369-1381.

12. Zhou, M., Wang, S.B., Yang, P.J., Huang, C.J., and Wang, X.C. (2018). Boron Carbon Nitride Semiconductors Decorated with CdS Nanoparticles for Photocatalytic Reduction of CO_2. ACS Catal. *8,* 4928-4936.

13. Zhao, Y.F., Chen, G.B., Bian, T., Zhou, C., Waterhouse, G.I.N., Wu, L.Z., Tung, C.H., Smith, L.J., O'Hare, D., and Zhang, T.R. (2015). Defect- Rich Ultrathin ZnAl-Layered Double Hydroxide Nanosheets for Efficient Photoreduction of CO_2 to CO with Water. Adv. Mater. *27,* 7824-7831.

14. Cao, S.W., Shen, B.J., Tong, T., Fu, J.W., and Yu, J.G. (2018). 2D/2D Heterojunction of Ultrathin MXene/Bi_2WO_6 Nanosheets for Improved Photocatalytic CO_2 Reduction. Adv. Funct. Mater. *28,* 1800136.

15. Chang, X.X., Wang, T., and Gong, J.L. (2016). CO_2 Photo-reduction: Insights into CO_2 Activation and Reaction on Surfaces of Photocatalysts. Energy Environ. Sci. *9,* 2177-2196.

16. Yang, M.Q., and Xu, Y.J. (2016). Photocatalytic Conversion of CO_2 over Graphene-based Composites: Current Status and Future Perspective. Nanoscale Horiz. *1,* 185-200.

17. Xiang, Q.J., Cheng, B., and Yu, J.G. (2015). Graphene-Based Photocatalysts for Solar-Fuel Generation. Angew. Chem. Int. Ed. *54,* 11350-11366.

18. Di, J., Xia, J.X., Li, H.M., and Liu, Z. (2017). Freestanding Atomically-thin Two-dimensional Materials beyond Graphene Meeting Photocatalysis: Opportunities and Challenges. Nano Energy *35,* 79-91.

19. Han, C., Zhang, N., and Xu, Y.J. (2016). Structural Diversity of Graphene Materials and Their Multifarious Roles in Heterogeneous Photocatalysis. Nano Today *11,* 351-372.

20. Zhang, J.S., Chen, Y., and Wang, X.C. (2015). Two-dimensional Covalent Carbon Nitride Nanosheets: Synthesis, Functionalization, and Applications. Energy Environ. Sci. *8,* 3092-3108.

21. Liu, J., Wang, H.Q., and Antonietti, M. (2016). Graphitic Carbon Nitride "reloaded": Emerging Applications beyond (Photo)catalysis. Chem. Soc. Rev. *45,* 2308-2326.

22. Lakhi, K.S., Park, D.H., Al-Bahily, K., Cha, W., Viswanathan, B., Choy, J.H., and Vinu, A. (2017). Mesoporous Carbon Nitrides: Synthesis, Functionalization, and Applications. Chem. Soc. Rev. *46,* 72-101.

23. Chen, Z., Savateev, A., Pronkin, S., Papaefthimiou, V., Wolff, C., Willinger, M.G., Willinger, E., Neher, D., Antonietti, M., and Dontsova, D. (2017). "The Easier the Better" Preparation of Efficient Photocatalysts-Metastable Poly(heptazine imide) Salts. Adv. Mater. *29,* 1700555.

24. Zhang, G., Lin, L., Li, G., Zhang, Y., Savateev, A., Zafeiratos, S., Wang, X., and Antonietti, M. (2018). Ionothermal Synthesis of

Triazine-Heptazine-Based Copolymers with Apparent Quantum Yields of 60 % at 420 nm for Solar Hydrogen Production from "Sea Water". Angew. Chem. Int. Ed. *57,* 9372-9376.

25. Zhang, G., Li, G., Lan, Z.A., Lin, L., Savateev, A., Heil, T., Zafeiratos, S., Wang, X., and Antonietti, M. (2017). Optimizing Optical Absorption, Exciton Dissociation, and Charge Transfer of a Polymeric Carbon Nitride with Ultrahigh Solar Hydrogen Production Activity. Angew. Chem. Int. Ed. *56,* 13445-13449.
26. Schwinghammer, K., Mesch, M.B., Duppel, V., Ziegler, C., Senker, J., and Lotsch, B.V. (2014). Crystalline Carbon Nitride Nanosheets for Improved Visible-light Hydrogen Evolution. J. Am. Chem. Soc. *136,* 1730-1733.
27. Miller, T.S., Suter, T.M., Telford, A.M., Picco, L., Payton, O.D., Russell-Pavier, F., Cullen, P.L., Sella, A., Shaffer, M.S.P., Nelson, J., *et al.* (2017). Single Crystal, Luminescent Carbon Nitride Nanosheets Formed by Spontaneous Dissolution. Nano Lett. *17,* 5891-5896.
28. Lin, L., Ren, W., Wang, C., Asiri, A.M., Zhang, J., and Wang, X. (2018). Crystalline Carbon Nitride Semiconductors Prepared at Different Temperatures for Photocatalytic Hydrogen Production. Appl. Catal. B-Environ. *231,* 234-241.

29. Lin, L., Ou, H., Zhang, Y., and Wang, X. (2016). Tri-s-triazine-Based Crystalline Graphitic Carbon Nitrides for Highly Efficient Hydrogen Evolution Photocatalysis. ACS Catal. *6,* 3921-3931.

30. Ou, H., Lin, L., Zheng, Y., Yang, P., Fang, Y., and Wang, X. (2017). Tri-s-triazine-Based Crystalline Carbon Nitride Nanosheets for an Improved Hydrogen Evolution. Adv. Mater. *29,* 1700008.

31. Liu, X., Fechler, N., and Antonietti, M. (2013). Salt Melt Synthesis of Ceramics, Semiconductors and Carbon Nanostructures. Chem. Soc. Rev. *42,* 8237-8265.

32. Wang, X.C., Maeda, K., Thomas, A., Takanabe, K., Xin, G., Carlsson, J.M., Domen, K., and Antonietti, M. (2009). A Metal-free Polymeric Photocatalyst for Hydrogen Production from Water under Visible Light. Nat. Mater. *8,* 76-80.

33. Kang, Y., Yang, Y., Yin, L.C., Kang, X., Liu, G., and Cheng, H.M. (2015). An Amorphous Carbon Nitride Photocatalyst with Greatly Extended Visible-Light-Responsive Range for Photocatalytic Hydrogen Generation. Adv. Mater. *27,* 4572-4577.

34. Moulder, J. F., Stickle, W. F., Sobol, P. E., and Bomben, K. D. (1992). Handbook of X-Ray Photoelectron Spectroscopy (Perkin-Elmer Corporation, Eden Prairie, MN, USA). pp. 41.

35. Kang, Y., Yang, Y., Yin, L.C., Kang, X., Wang, L., Liu, G., and Cheng, H.M. (2016). Selective Breaking of Hydrogen Bonds of Layered Carbon Nitride for Visible Light Photocatalysis. Adv. Mater. *28,* 6471-6477.

36. Fu, J., Zhu, B., Jiang, C., Cheng, B., You, W., and Yu, J. (2017). Hierarchical Porous O-Doped g-C_3N_4 with Enhanced Photocatalytic CO_2 Reduction Activity. Small *13,* 1603938.

37. Barrio, J., Lin, L., Amo-Ochoa, P., Tzadikov, J., Peng, G., Sun, J., Zamora, F., Wang, X., and Shalom, M. (2018). Unprecedented Centimeter-Long Carbon Nitride Needles: Synthesis, Characterization and Applications. Small *14,* 1800633.

38. Yu, H., Shi, R., Zhao, Y., Bian, T., Zhao, Y., Zhou, C., Waterhouse, G.I.N., Wu, L.Z., Tung, C.H., and Zhang, T. (2017). Alkali-Assisted Synthesis of Nitrogen Deficient Graphitic Carbon Nitride with Tunable Band Structures for Efficient Visible-Light-Driven Hydrogen Evolution. Adv. Mater. *29,* 1605148.

39. Xu, J., Wang, H., Zhang, C., Yang, X., Cao, S., Yu, J., and Shalom, M. (2017). From Millimeter to Subnanometer: Vapor-Solid Deposition of Carbon Nitride Hierarchical Nanostructures Directed by Supramolecular Assembly. Angew. Chem. Int. Ed. *56,* 8426-8430.

40. Li, Y., Ouyang, S., Xu, H., Wang, X., Bi, Y., Zhang, Y., and Ye, J. (2016). Constructing Solid-Gas-Interfacial Fenton Reaction over

Alkalinized-C_3N_4 Photocatalyst To Achieve Apparent Quantum Yield of 49% at 420 nm. J. Am. Chem. Soc. *138,* 13289-13297.

41. Xiong, T., Cen, W., Zhang, Y., and Dong, F. (2016). Bridging the g-C_3N_4 Interlayers for Enhanced Photocatalysis. ACS Catal. *6,* 2462-2472.
42. Niu, P., Zhang, L.L, Liu, G., and Cheng, H.M. (2012). Graphene-Like Carbon Nitride Nanosheets for Improved Photocatalytic Activities. Adv. Funct. Mater. *22,* 4763–4770.
43. Li, J., Kuang, D., Feng, Y., Zhang, F., Xu, Z., and Liu, M. (2012). A Graphene Oxide-based Electrochemical Sensor for Sensitive Determination of 4-nitrophenol. J. Hazard. Mater. *201-202,* 250-259.
44. Savateev, A., Pronkin, S., Epping, J.D., Willinger, M.G., Wolff, C., Neher, D., Antonietti, M., and Dontsova, D. (2017). Potassium Poly(heptazine imides) from Aminotetrazoles: Shifting Band Gaps of Carbon Nitride-like Materials for More Efficient Solar Hydrogen and Oxygen Evolution. ChemCatChem *9,* 167-174.
45. Lotsch, B.V., Döblinger, M., Sehnert, J., Seyfarth, L., Senker, J., Oeckler, O., and Schnick, W. (2007). Unmasking Melon by a Complementary Approach Employing Electron Diffraction, Solid-State NMR Spectroscopy, and Theoretical Calculations-Structural Characterization of a Carbon Nitride Polymer. Chem. Eur. J. *13,* 4969–4980.

46. Jürgen, B., Irra, E., Senker, J., Kroll, P., Müller, H., Schnick, W. (2003), Melem (2,5,8-Triamino-tri-s-triazine), an Important Intermediate during Condensation of Melamine Rings to Graphitic Carbon Nitride: Synthesis, Structure Determination by X-ray Powder Diffractometry, Solid-State NMR, and Theoretical Studies. J. Am. Chem. Soc. *125,* 10288–10300.

47. Wirnhier, E., Mesch M.B., Senker J., and Schnick, W. (2013). Formation and Characterization of Melam, Melam Hydrate, and a Melam–Melem Adduct. Chem. Eur. J. *19,* 2041–2049.

48. Dontsova, D., Pronkin, S., Wehle, M., Chen, Z., Fettkenhauer, C., Clavel, G., and Antonietti, M. (2015). Triazoles: A New Class of Precursors for the Synthesis of Negatively Charged Carbon Nitride Derivatives. Chem. Mater. *27,* 5170-5179.

49. Gu, W., Lu, F., Wang, C., Kuga, S., Wu, L., Huang, Y., and Wu, M. (2017), Face-to-Face Interfacial Assembly of Ultrathin g-C_3N_4 and Anatase TiO_2 Nanosheets for Enhanced Solar Photocatalytic Activity. ACS Appl. Mater. Interfaces *9,* 28674−28684.

50. Yu, X., Zhao, Z., Sun, D., Ren, N., Yu, J., Yang, R., Liu, H. (2018). Microwave-assisted Hydrothermal Synthesis of Sn_3O_4 Nanosheet/rGO Planar Heterostructure for Efficient Photocatalytic Hydrogen Generation. Appl. Catal. B-Environ. *227,* 470-476.

51. Low, J., Zhang, L., Tong, T., Shen, B., Yu, J. (2018), TiO_2/MXene Ti_3C_2 Composite with Excellent Photocatalytic CO_2 Reduction Activity. J. Catal. *361,* 255-266.

52. Zhang, L., Reisner, E., and Baumberg, J. (2014), Al-doped ZnO Inverse Opal Networks as Efficient Electron Collectors in $BiVO_4$ Photoanodes for Solar Water Oxidation. Energy Environ. Sci. *7,* 1402–1408.

53. Bell, N.J., Ng, Y.H., Du, A., Coster, H., Smith, S.C., and Amal, R. (2011). Understanding the Enhancement in Photoelectrochemical Properties of Photocatalytically Prepared TiO_2-Reduced Graphene Oxide Composite. J. Phys. Chem. C *13,* 6004-6009.

54. Pan, H., Ritter, J.A., and Balbuena, P.B. (1998). Examination of the Approximations Used in Determining the Isosteric Heat of Adsorption from the Clausius-Clapeyron Equation. Langmuir *14*, 6323-6327.

55. Ren, X., Li, H., Chen, J., Wei, L., Modak, A., Yang, H., and Yang, Q. (2017). N-doped Porous Carbons with Exceptionally High CO_2 Selectivity for CO_2 Capture. Carbon *114*, 473-481.

56. Tian, Z., Fechler, N., Oschatz, M., Heil, T., Schmidt, J., Yuan, S., and Antonietti, M. (2018). $C_2N_xO_{1-x}$ Framework Carbons with Defined Microporosity and Co-doped Functional Pores. J. Mater. Chem. A *6*, 19013-19019.

57. Lu, W., Yuan, D., Sculley, J., Zhao, D., Krishna, R., and Zhou, H.C. (2011). Sulfonate-grafted Porous Polymer Networks for Preferential

CO_2 Adsorption at Low Pressure. J. Am. Chem. Soc. *133*, 18126-18129.

58. Ma, H., Ren, H., Zou, X., Meng, S., Sun, F., and Zhu, G. (2014). Post-metalation of Porous Aromatic Frameworks for Highly Efficient Carbon Capture from CO_2 + N_2 and CH_4 + N_2 Mixtures. Polym. Chem. *5*, 144-152.

59. Zhang, G., Wei, G., Liu, Z., Oliver, S.R.J., and Fei, H. (2016). A Robust Sulfonate-Based Metal–Organic Framework with Permanent Porosity for Efficient CO_2 Capture and Conversion. Chem. Mater. *28*, 6276-6281.

60. Caskey, S.R., Wong-Foy, A.G., and Matzger, A.J. (2008). Dramatic Tuning of Carbon Dioxide Uptake via Metal Substitution in a Coordination Polymer with Cylindrical Pores. J. Am. Chem. Soc. *130*, 10870-10871.

61. Enujekwu, F.M., Ezeh, C.I., George, M.W., Xu, M.X., Do, H., Zhang, Y., Zhao, H., and Wu, T. (2019). A Comparative Study of Mechanisms of the Adsorption of CO_2 Confined within Graphene–MoS_2 Nanosheets: a DFT Trend Study. Nanoscale Adv. *1*, 1442-1451

62. Oschatz, M., and Antonietti, M. (2018). A Search for Selectivity to Enable CO_2 Capture with Porous Adsorbents. Energy Environ. Sci. *11*, 57-70.

63. Mao, J., Peng, T.Y., Zhang, X.H., Li, K., Ye, L.Q., Zan, L. (2013). Effect of graphitic carbon nitride microstructures on the activity and selectivity of photocatalytic CO_2 reduction under visible light. Catal. Sci. Technol. *3,* 1253-1260.

64. Tu, W.G., Zhou, Y., Liu, Q., Yan, S.C., Bao, S.S., Wang, X.Y., Xiao, M., Zou, Z.G. (2013). An In Situ Simultaneous Reduction-Hydrolysis Technique for Fabrication of TiO_2-Graphene 2D Sandwich-Like Hybrid Nanosheets: Graphene-Promoted Selectivity of Photocatalytic-Driven Hydrogenation and Coupling of CO_2 into Methane and Ethane. Adv. Funct. Mater. *23,* 1743-1749.

65. Sorcar, S., Thompson, J., Hwang, Y., Park, Y.H., Majima, T., Grimes, C.A., Durrant, J. R., In, S. (2018). High-rate Solar-light Photoconversion of CO_2 to Fuel: Controllable Transformation from C1 to C2 Products. Energy Environ. Sci. *11,* 3183-3193.

66. Zhu, M.S., Kim, S., Mao, L., Fujitsuka, M., Zhang, J.Y., Wang, X.C., Majima, T. (2017). Metal-Free Photocatalyst for H_2 Evolution in Visible to Near-Infrared Region: Black Phosphorus/Graphitic Carbon Nitride. J. Am. Chem. Soc. *139,* 13234-13242.

67. Yang, P., and Tarascon, J.M. (2012). Towards Systems Materials Engineering. Nat. Mater. *11,* 560-563.

68. Kunz, L.Y., Diroll, B.T., Wrasman, C.J., Riscoe, A.R., Majumdar, A., Cargnello, M. (2019). Artificial Inflation of Apparent Photocatalytic

Activity Induced by Catalyst-mass-normalization and a Method to Fairly Compare Heterojunction Systems. Energy Environ. Sci. *12,* 1657-1667.

69. Razip, F., Sun, L.Q., Wang, Y., Zhang, X.L., Humayun, M., Ali, S., Bai, L.L., Qu, Y., Yu, H.T., Jing, L.Q. (2017). Synthesis of Large Surface-Area g-C_3N_4 Comodifed with MnOx and Au-TiO_2 as Effcient Visible-Light Photocatalysts for Fuel Production. Adv. Energy Mater. 1701580.

70. Wang, Y., Zhang, Z.Z., Zhang, L.N., Luo, Z.B., Shen, J.N., Lin, H.X., Long, J.L., Wu, J.C.S., Fu, X.Z., Wang, X.X., and Li, C. (2018). Visible-Light Driven Overall Conversion of CO_2 and H_2O to CH_4 and O_2 on 3D-SiC@2D-MoS_2 Heterostructure. J. Am. Chem. Soc. *140,* 14595-14598.

71. Xu, Y.X., Bai, H., Lu, G.W., Li, C., and Shi, G.Q. (2008). Flexible Graphene Films via TheFiltration of Water-soluble Noncovalent Functionalized Graphene Sheets. J. Am. Chem. Soc. *130*, 5856-5857.

Supplemental Experimental Procedures

Synthesis of CNNA/rGO-R4:

Firstly, 3 g of melamine powder was calcined at 500 °C for 4 h with a heating rate of 10 °C/min under N_2 atmosphere. After cooling to room temperature, the obtained sample was ground into powder and then mixed with 3 mL of GO aqueous solution (1.0 g/L). Subsequently, the mixture was dried at 80 °C overnight and then ground with KCl (2.75 g) and LiCl (2.25 g) on the hot plate at 100 °C. After that, the mixture was heated in N_2 atmosphere at a heating rate of 5 °C/min to 550 °C for 4 h. The final product was washed with boiling distilled water, and then followed by drying at 60 °C overnight in a vacuum oven.

Synthesis of bCN-K:

3 g of melamine powder ground with KCl (2.75 g) on the hot plate at 100 °C. After that, the mixture was calcined at 500 °C for 4 h with a heating rate of 10 °C/min under N_2 atmosphere. The final product was washed with boiling distilled water, and then followed by drying at 60 °C overnight in a vacuum oven. This sample was denoted as bCN-K.

Characterization:

The X-ray diffraction (XRD) patterns were recorded on a Bruker D8 Advance instrument with Cu-Kα as the radiation source. The chemical compositions and optical performance of samples were characterized by X-ray photoelectron spectroscopy (VG ESCALAB 210, U.K.), Fourier transform infrared (FTIR, Nicolet iS50, TMO, USA) spectroscopy, and UV-visible spectrophotometer (UV-2600, Shimadzu, Japan). The morphologies of the as-obtained samples were characterized by a double-corrected JEOL ARM200F transmission electron microscope equipped with a cold field emission gun, and a JSM-7500 field emission scanning electron microscope. The specific surface area and pore structure were analyzed by N_2 adsorption–desorption isotherms using a Micromeritics ASAP 2020 Apparatus (Micromeritics Instruments, USA). The valence band positions were determined by ultraviolet photoelectron spectroscopy (UPS) on the VG ESCALAB 210 spectrometer. The elemental analysis was performed on an elemental analyzer (Vario EL cube, Elementar, Germany) and an atomic absorption spectrometer with a continuous light source (contrAA800, Jena, Germany). Solid state NMR spectra were recorded with a Bruker Avance 400 MHz spectrometer operating at 100.56 MHz for ^{13}C, 40.53 MHz for ^{15}N using a 4 mm MAS HX double resonance probe. The spectra were measured using contact time of 2.0 ms for ^{13}C and 4.0 ms for ^{15}N and recycle delays of 2 and 5 s, respectively. A $\pi/2$ pulse length of 5 µs was applied for ^{13}C and a $\pi/6$ pulse length of 2 µs for ^{15}N, using a recycle delay of 90 s in both cases. All ^{13}C spectra are referenced to external TMS at 0 ppm using adamantane as a secondary reference. All ^{15}N spectra are referenced to neat nitromethane CH_3NO_2 at 0 ppm using solid NH_4Cl as a secondary reference. Room temperature photoluminescence (PL) emission spectra of the samples were collected on a Hitachi F-700 fluorescence spectrophotometer at an excitation wavelength of 325 nm. Time-resolved transient photoluminescence (TRPL) spectra were recorded on a fluorescence lifetime spectrophotometer (FLS920, Edinburgh, UK) at an excitation wavelength of 325 nm.

Photoelectrochemical measurement:

The photoelectrochemical measurements for the as-obtained samples were performed by a CHI660 electrochemical workstation (CHENHUA, China) using a standard three-electrode system. The sample was coated onto FTO glass, which was used as working electrode. Platinum wire, Ag/AgCl (saturated KCl) and 0.5 M Na_2SO_4 solution (pH = 6.8) were used as counter electrode, reference electrode and electrolyte, respectively. The transient photocurrent response test was performed by using a 3 W LED (420 nm) as light source. The open-circuit voltages were set as the initial bias voltages in the electrochemical impedance spectroscopy and transient photocurrent tests.

Quantum yield measurement:

The photochemical quantum yield was measured under the same photocatalytic reaction condition except that four 420-nm LEDs (3 W) (Shenzhen LAMPLIC Science Co. Ltd., China) were used as light sources to trigger the photocatalytic reaction, instead of the xenon arc lamp. The LEDs were positioned on the top of the reactor and the focused intensity on the reactor for total of them was ca. 5100 μW/cm^2. Meanwhile, the catalyst film area in reactor (circle, r = 2.5 cm) was 19.63 cm^2 and the photon energy (at 420 nm wavelength) was 6.00 × 10^{-19} J. Thus, quantum yields of CO, CH_4, CH_3OH and C_2H_5OH can be calculated using the following equations. Two, eight, six and twelve electrons are required to convert CO_2 to CO, CH_4, CH_3OH and C_2H_5OH, respectively.

$$\Phi_{co}(\%) = \frac{2\ mol\ of\ CO\ yield}{moles\ of\ photon\ absorbed\ by\ catalyst} \times 100\% \quad (1)$$

$$\Phi_{CH_4}(\%) = \frac{8\ mol\ of\ CH_4\ yield}{moles\ of\ photon\ absorbed\ by\ catalyst} \times 100\% \quad (2)$$

$$\Phi_{CH_3OH}(\%) = \frac{6\ mol\ of\ CH_3OH\ yield}{moles\ of\ photon\ absorbed\ by\ catalyst} \times 100\% \quad (3)$$

$$\Phi_{C_2H_5OH}(\%) = \frac{12\ mol\ of\ C_2H_5OH\ yield}{moles\ of\ photon\ absorbed\ by\ catalyst} \times 100\% \quad (4)$$

$$\Phi_{total} = \Phi_{CO} + \Phi_{CH_4} + \Phi_{CH_3OH} + \Phi_{C_2H_5OH} \quad (5)$$

Turnover number (TON) calculation:

The turnover number (TON) is defined as mole of reacted electrons from the system per mole of catalyst after irradiation at a certain time. Therefore, TON of CNNA/rGO (based on the amount of the rGO) for photocatalytic CO_2 reduction under simulated solar light irradiation with 4 hours can be calculated from following eq.(6).

$$\mathrm{TON} = \frac{Number\ of\ reacted\ electrons}{Amount\ of\ catalyst} \quad (6)$$

Table S1 The comparison and contrast of binding energy of various elements for CNNA and common PTI and polymeric CN materials from other literatures.

Sample	Binding energy (eV)					Ref.
	C (1s)	N (1s)	Li (1s)	K (2p)	Cl (2p)	
Bulk CN	283.8 287.0 287.7	398.1 399.6 403.1	—	—	—	1
Bulk CN	284.6 288.1 288.8	398.6 399.6 400.7 404.4	—	—	—	2
Bulk poly(triazine imide) (PTI)	284.5 286.2 287.7	398.2 399.8	55.1	Not given	197.7 199.4	3
Amorphous poly(triazine imide) (aPTI)	284.6 286.1 287.8	398.5 399.8 403.6	Not given	Not given	Not given	4
CNNA	284.8 286.5 288.3	398.7 400.4 401.3 404.1	No signal	293.0 295.8	197.8 199.6	This work

Table S2. Elemental analysis of CNNA and CNNA/rGO.

Sample	C (wt%)	N (wt%)	C/N molar ratio
CNNA	26.97	43.27	0.73
CNNA/rGO	29.85	42.79	0.81

Table S3. The content of K, Li, Cl tested by atomic absorption spectrograph over CNNA and CNNA/rGO.

Sample	Li (wt%)	K (wt%)	Cl (wt%)
CNNA	0.041	4.63	0.051
CNNA/rGO	0.022	3.82	0.037

Table S4. Specific surface area and pore volume of bCN, CNNA and CNNA/rGO.

Sample	S_{BET} ($m^2\ g^{-1}$)	Pore volume ($cm^3\ g^{-1}$)
bCN	7	0.02
CNNA	64	0.20
CNNA/rGO	55	0.19

Table S5. The fitted parameters obtained from decay curves of various samples.[a]

Sample	τ_1 (ns) (Rel. %)	τ_2 (ns) (Rel. %)	τ_A/ns
bCN	2.56 (39.86)	8.14 (60.14)	7.18
CNNA	2.96 (34.04)	9.74 (65.96)	8.82
CNNA/rGO	4.51 (26.07)	13.53 (73.93)	12.58

[a]The decay curves of bCN, CNNA and CNNA/rGO are well fitted by bi-exponential decay equation ($y = y_0 + A_1 \exp(-t/\tau_1) + A_2 \exp(-t/\tau_2)$). The average lifetime (τ_A) of the fluorescence in each sample is calculated based on the equation ($\tau_A = (A_1\tau_1^2 + A_2\tau_2^2)/(B\tau_1 + B_2\tau_2)$). τ_1 and τ_2 represent the short lifetime and the long lifetime, and A_1 and A_2 are the pre-exponential factors of decay curves.

Table S6. The yield of gas products (μmol h^{-1} g^{-1}) of gas-phase CO_2 photoreduction over various photocatalysts, without any sacrificial agent.

Samples	**CH_4**	**CO**	**CH_3OH**	**C_2H_5OH**	**Total CO_2 conversion**	**H_2**
bCN	0.43	0.46	0.89	0.33	2.11	trace
CNNA	1.74	0.77	trace	0.52	3.03	trace
CNNA/rGO-R1	3.63	1.20	trace	0.68	5.51	0.21
CNNA/rGO	4.30	6.65	0.53	1.15	12.63	1.93
CNNA/rGO-R2	4.07	5.56	0.22	0.74	10.59	0.77
CNNA/rGO-R3	3.47	4.06	trace	0.65	8.18	0.19
CNNA/rGO-R4	1.81	0.62	trace	0.63	3.06	0.14
bCN-K	0.61	0.54	1.27	0.46	2.88	0.17
bCN+KCl	0.45	0.49	0.95	0.37	2.26	0.10

Table S7. Comparison of gas-phase CO_2 photoreduction over carbon nitride-based photocatalysts in the absence of any sacrificial agent reported in literatures.

Photocatalysts and total mass	Light source	Products and yield ($\mu mol\ g^{-1}\ h^{-1}$)	Ref.
g-C_3N_4 (40 mg)	300 W Xe lamp (λ > 200 nm)	CO (2.1) CH_4 (0.24)	5
Tubular g-C_3N_4 (30 mg)	300 W Xe lamp	CO (1.79)	6
Mesoporous g-C_3N_4 (50 mg)	300 W Xe lamp	CO (3.27)	7
Phosphorus-doped g-C_3N_4 (50 mg)	300 W Xe lamp	CO (2.37) CH_4 (1.81)	8
Oxygen-doped g-C_3N_4 (50 mg)	350 W Xe lamp (λ > 420 nm)	CH_3OH (0.88)	9
MnO_2/g-C_3N_4 (50 mg)	300 W Xe lamp	CO (3.4)	10
BiOI/g-C_3N_4 (100 mg)	300 W Xe lamp (λ > 400 nm)	CO (4.86) CH_4 (0.18)	11
Bi_2WO_6/g-C_3N_4 (100 mg)	300 W Xe lamp (λ > 420 nm)	CO (5.19)	12
SnS_2/g-C_3N_4 (50 mg)	300 W Xe lamp (λ > 420 nm)	CH_4 (0.64) CH_3OH (2.3)	13
ZnO/g-C_3N_4 (10 mg)	300 W Xe lamp	CH_3OH (0.6)	14
Carbon/g-C_3N_4 (100 mg)	500 W Xe lamp	CO (2.51) CH_4 (1.39)	15
Ru/g-C_3N_4 (15 mg)	300 W Xe lamp (420-780 nm)	CO (4.78) CH_4 (0.78)	16
Pt/g-C_3N_4 (50 mg)	300 W Xe lamp (λ > 420 nm)	CH_4 (0.8)	17
Au/g-C_3N_4/ZIF-9 (50 mg)	300 W Xe lamp	CO (7.66)	18
NiAl-LDH/g-C_3N_4 (50 mg)	300 W Xe lamp (λ > 420 nm)	CO (8.2)	19

Table S8. Comparison of gas-phase CO_2 photoreduction over graphene-based photocatalysts in the absence of any sacrificial agent reported in literatures.

Photocatalysts and total mass	Light source	Products and yield ($\mu mol\ g^{-1}\ h^{-1}$)	Ref.
$Fe_2V_4O_{13}$/RGO/CdS (25 mg)	300 W Xe lamp (λ > 420 nm)	CH_4 (2.04)	20
Amine-functionalized graphene/CdS (50 mg)	300 W Xe lamp (λ > 420 nm)	CH_4 (2.84)	21
Cu/GO (100 mg)	300 W Xe lamp	CH_3OH (2.94) CH_3CHO (3.88)	22
1,1'-bi(2-naphthalene) functionalized graphene quantum dots (100 mg)	300 W Xe lamp (λ > 420 nm)	CH_3OH (0.695)	23
CdS/rGO (100 mg)	300 W Xe lamp (λ > 420 nm)	CH_4 (2.51)	24
TiO_2/graphene (10 mg)	300 W Xe lamp	CO (8.91) CH_4 (1.14)	25
Ag_2CrO_4/g-C_3N_4/GO (100 mg)	300 W Xe lamp	CO+CH_4 (0.35)	26
WO_3/graphene (100 mg)	300 W Xe lamp (λ > 400 nm)	CH_4 (1.11)	27

Table S9. Details of the quantum efficiency over CNNA/rGO.

Product	**yield**[a] **(μmol g^{-1} h^{-1})**	**The quantum efficiency (Φ) (%)**
CH_4	1.38	0.11
CO	3.67	0.074
CH_3OH	0.13	0.0078
C_2H_5OH	0.50	0.062

[a]Reaction conditions: photocatalyst, 100 mg; light source, 420-nm LEDs.

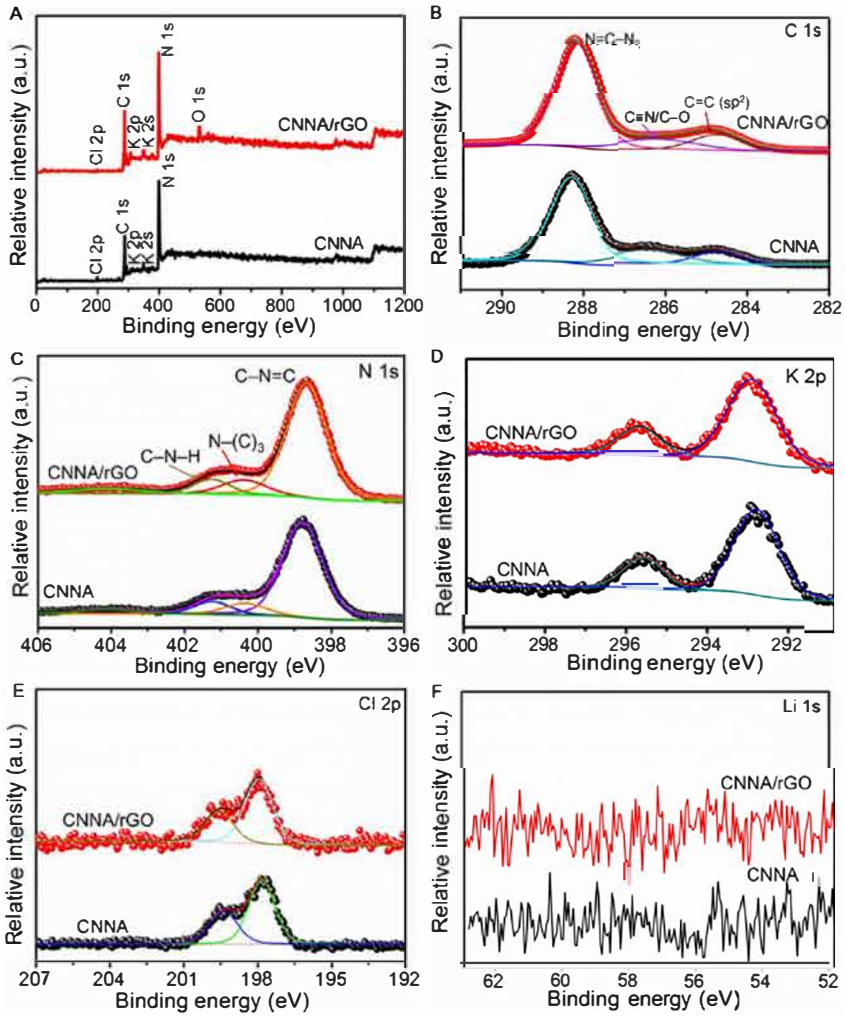

Figure S1. XPS survey spectra (A), high-resolution spectra of the C 1s (B) and N 1s (C) K 2p (D), Cl 2p (E) and Li 1s (F) for CNNA and CNNA/rGO.

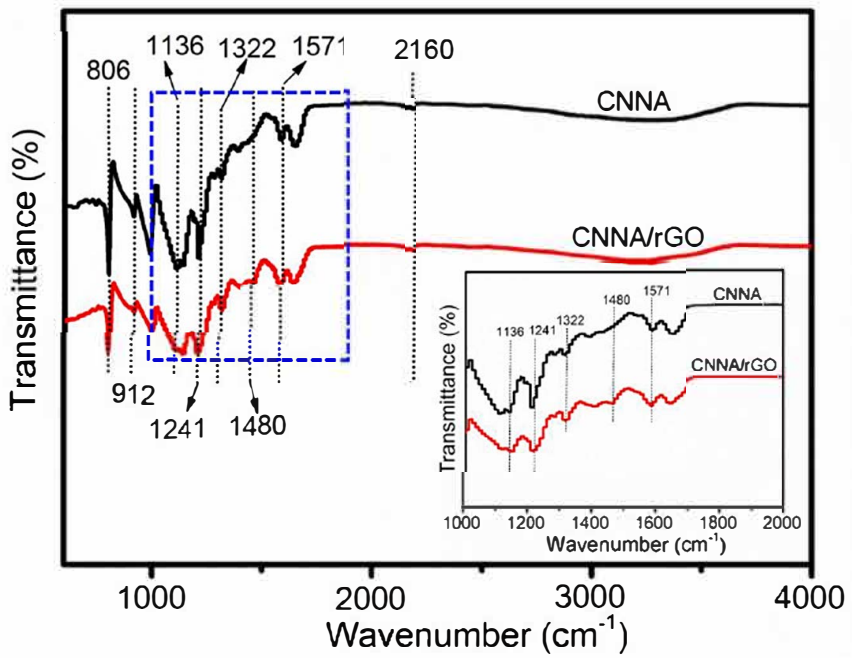

Figure S2. FTIR spectra of CNNA and CNNA/rGO. For both CNNA and CNNA/rGO. The broad peaks in the region of 3000–3500 cm^{-1} correspond to the stretching vibration modes of amino groups. The peak at 2160 cm^{-1} is assigned to terminal cyano groups C≡N. Additionally, the location of peaks at 1571, 1322, 1241, 1136, 912 and 806 cm^{-1} correspond to the typical absorption peaks of tri-s-triazine derivatives and triazine units. A new peak appeared at 1480 cm^{-1} for the spectrum of CNNA/rGO, which can be assigned to the skeletal vibration of rGO.

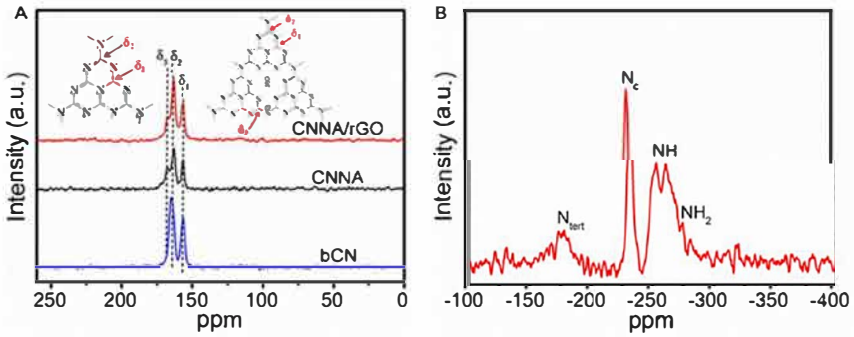

Figure S3. ^{13}C CP-MAS NMR spectra of bCN, CNNA and CNNA/rGO (A); ^{15}N CP-MAS NMR spectrum of the CNNA/rGO (B).

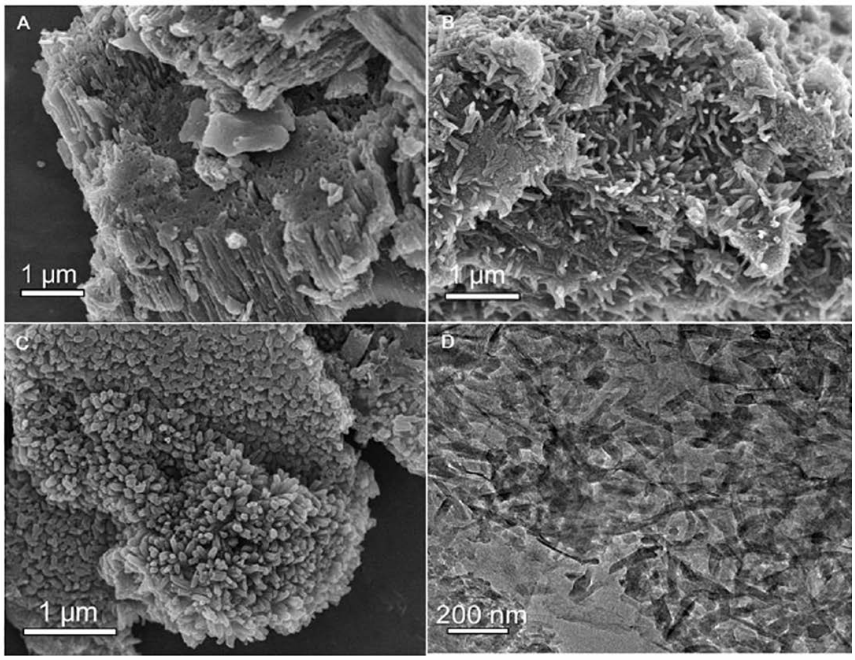

Figure S4. SEM images of (A) bCN, (B) CNNA, (C) CNNA/rGO. (D) TEM image of CNNA/rGO after continuous sonication.

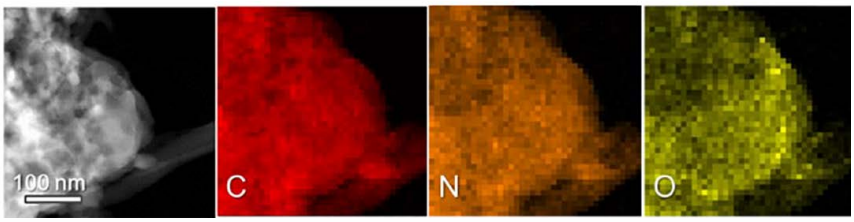

Figure S5. Elemental mapping images of C, N and O for CNNA/rGO.

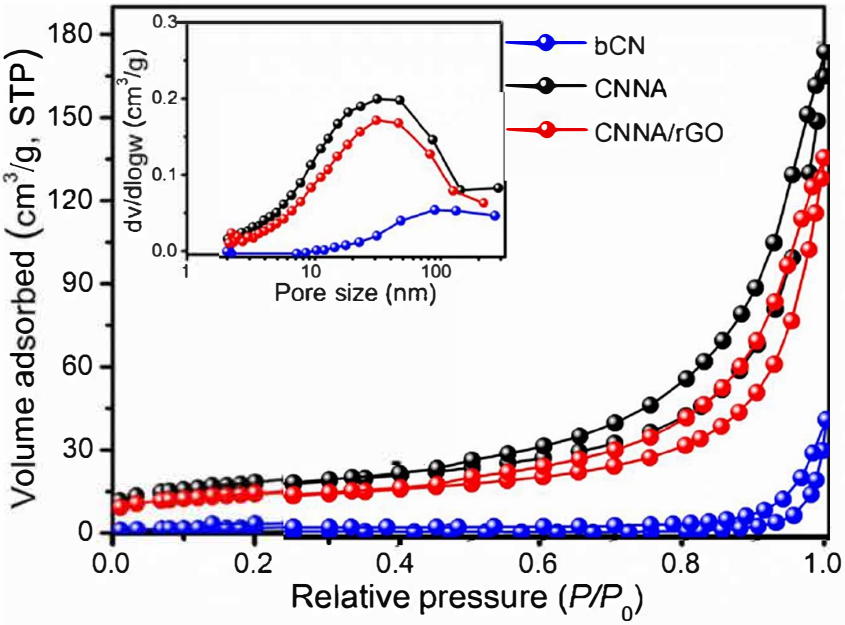

Figure S6. N_2 adsorption–desorption isothermal and the corresponding pore size distribution curves (inset) of bCN, CNNA and CNNA/rGO. The pore size distribution was obtained by the BJH method using adsorption branch data. The three samples show type IV adsorption–desorption isotherm according to the International Union of Pure and Applied Chemistry (IUPAC) classification. The isotherms of CNNA and CNNA/rGO shift upward compared with that of bCN, indicating the enlarged BET surface area of CNNA and CNNA/rGO. Additionally, the hysteresis loops of type H3 for these samples suggest the existence of narrow slit-shaped pores. The inset reveals the significantly increased mesopores and macropores for CNNA and CNNA/rGO, due to the inter-particle or nanorod aggregation.

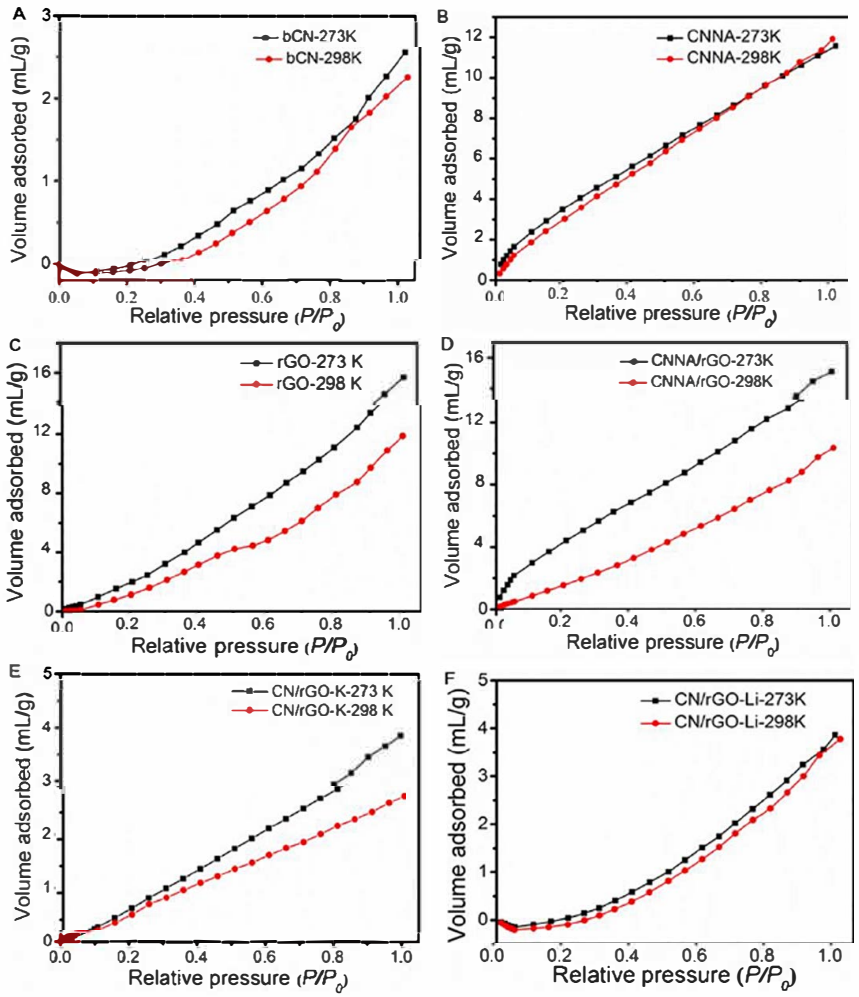

Figure S7. CO_2 adsorption isotherms on bCN (A), CNNA (B), rGO (C), CNNA/rGO (D), CN/rGO-K (E) and CN/rGO-Li (F) at 273K and 298K, respectively.

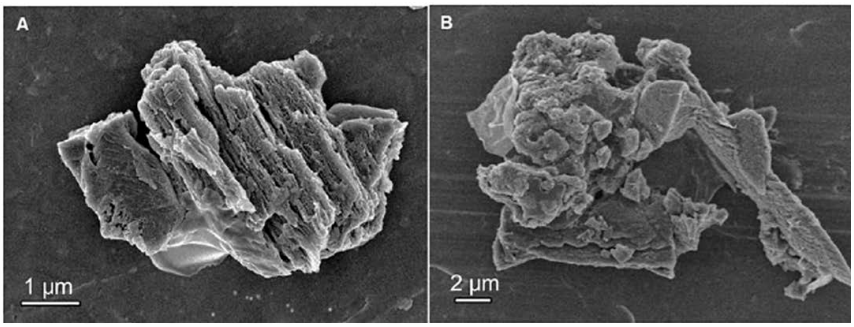

Figure S8. SEM images of CN/rGO-K (A) and CN/rGO-Li (B).

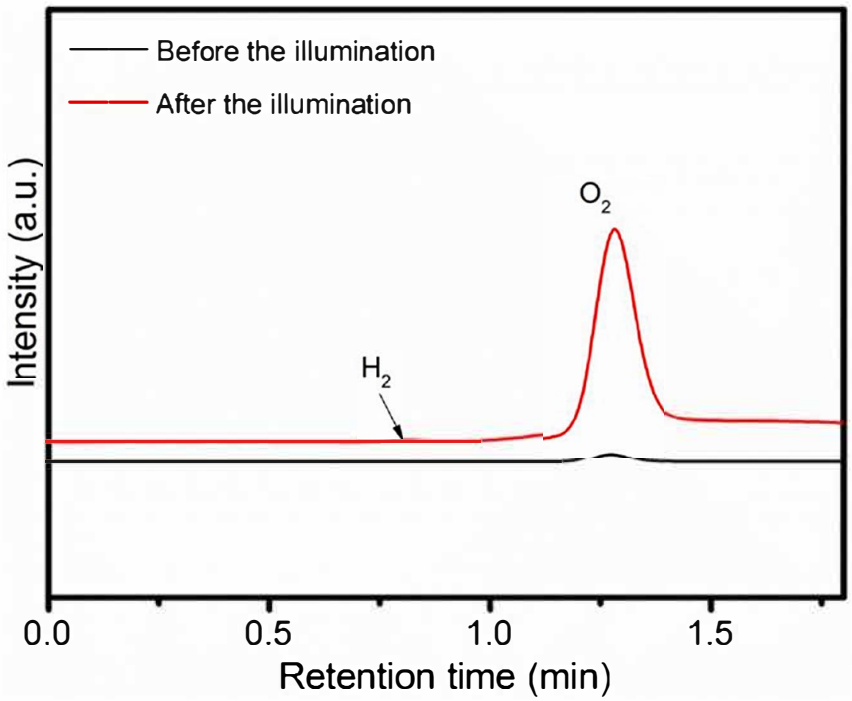

Figure S9. The GC spectra of resulting O_2 after photocatalytic CO_2-reduction reaction over CNNA/rGO.

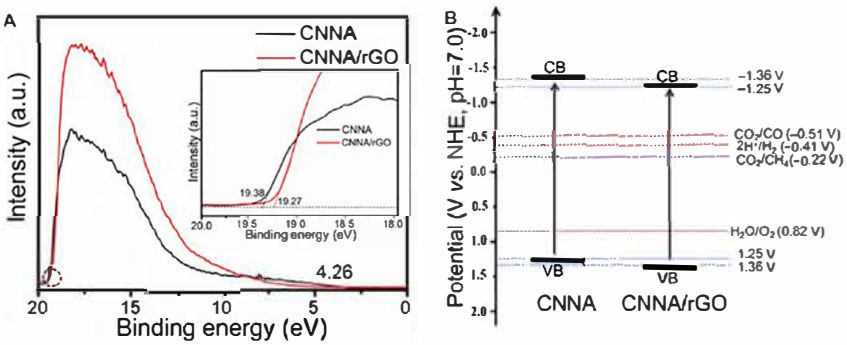

Figure S10. UPS spectra of CNNA and CNNA/rGO (A) and band positions of CNNA and CNNA/rGO (B). The valence band positions (E_{VB}) of CNNA and CNNA/rGO are calculated to be 1.25, and 1.36 V, respectively (vs. NHE, pH=7) by subtracting the width of the He I UPS spectrum from the exciting energy (21.22 eV).

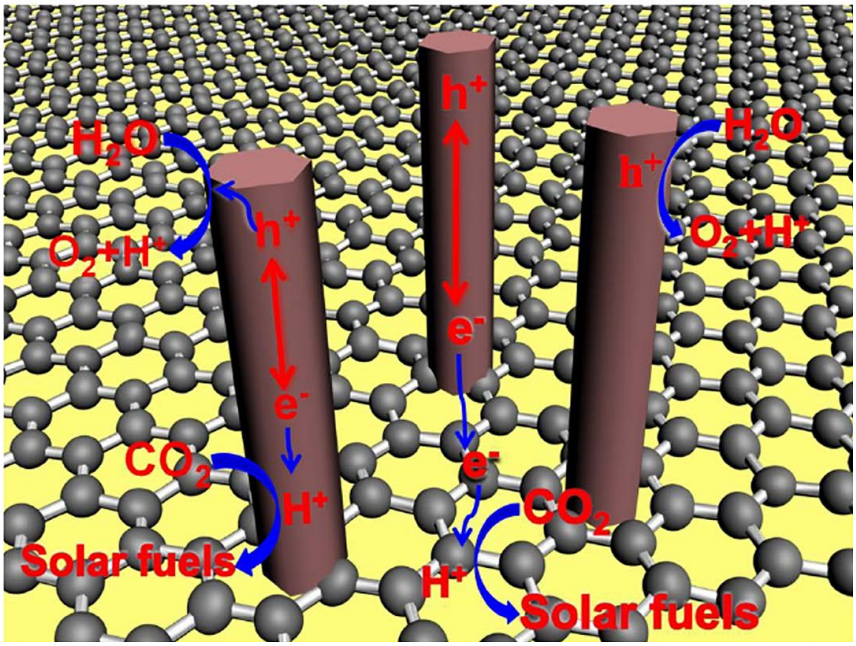

Figure S11. The scheme of photocatalytic CO_2 reduction mechanism on CNNA/rGO.

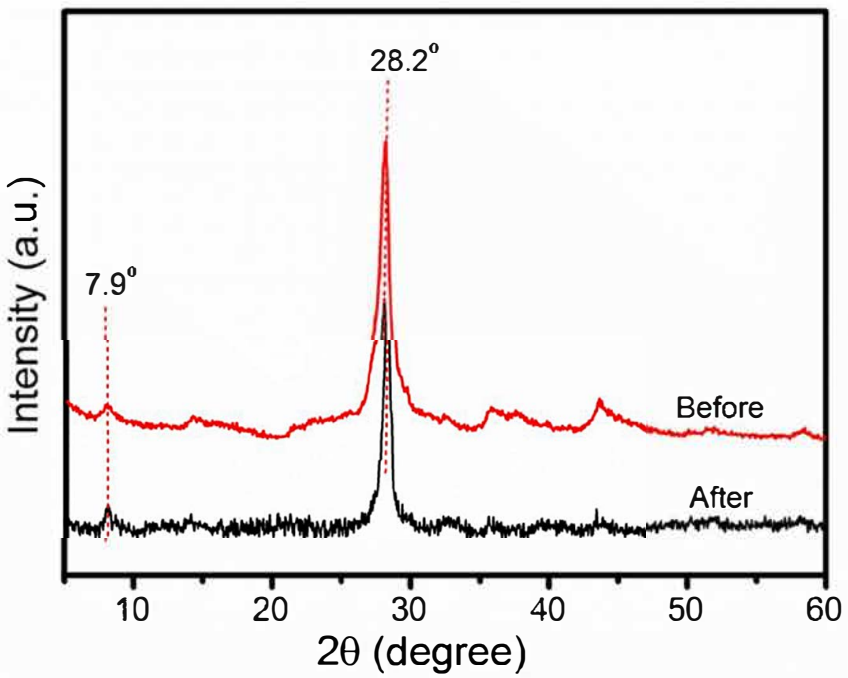

Figure S12. XRD patterns of CNNA/rGO before and after the stability measurement.

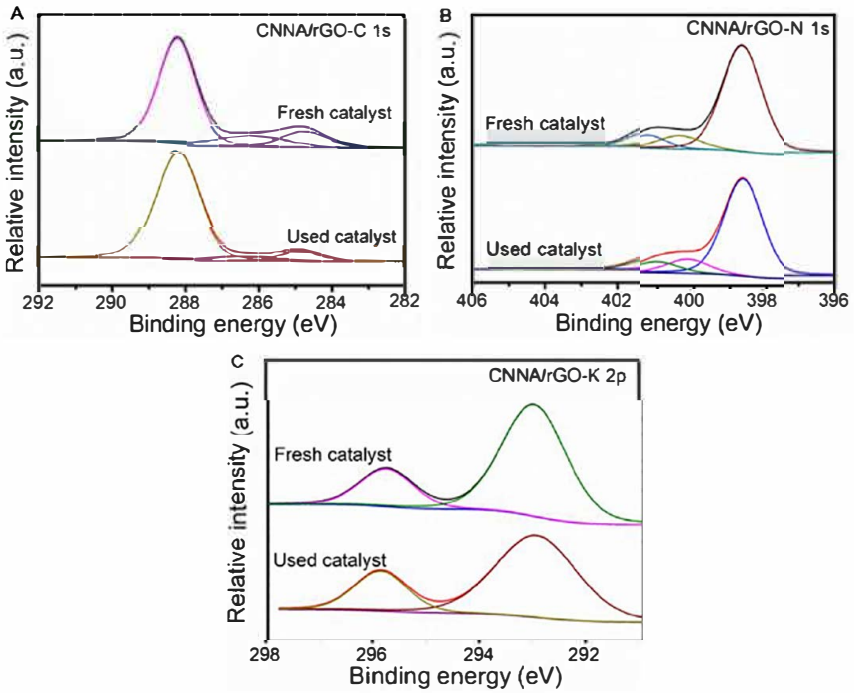

Figure S13. High-resolution XPS spectra of C 1s (A), N 1s (B) and K 2p (C) of CNNA/rGO before and after the stability measurement.

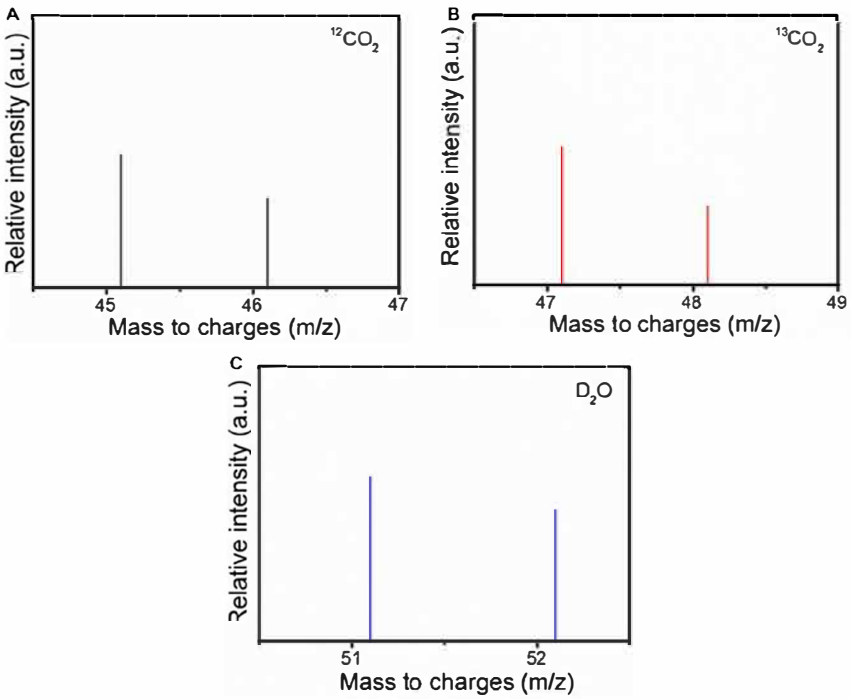

Figure S14. GC-MS analysis of the produced C_2H_5OH over CNNA/rGO using $^{12}CO_2$ to react with H_2O (A), $^{13}CO_2$ to react with H_2O (B) and $^{12}CO_2$ to react with D_2O (C), respectively.

Supplemental References

1. Niu, P., Zhang, L.L., Liu, G., and Cheng, H.M. (2012). Graphene-Like Carbon Nitride Nanosheets for Improved Photocatalytic Activities. Adv. Funct. Mater. *22,* 4763-4770.
2. Zhou, Y., Zhang, L., Huang, W., Kong, Q., Fan, X., Wang, M., and Shi, J. (2016). N-doped Graphitic Carbon-incorporated g-C_3N_4 for Remarkably Enhanced Photocatalytic H_2 Evolution under Visible Light. Carbon *99,* 111-117.
3. Liu, L., Shi, Q., Yin, N., Zhang, M., Liu, X., Zheng, H., Wu, G., Chen, P. (2017). Enhanced Room-temperature Ferromagnetic Properties in Ultrathin Two-dimensional Metal-free Poly(triazine imide) Nanosheets. Carbon *124,* 486-491.
4. Schwinghammer, K., Tuffy, B., Mesch, M.B., Wirnhier, E., Martineau, C., Taulelle, F., Schnick, W., Senker, J., and Lotsch, B.V. (2013). Triazine-based Carbon Nitrides for Visible-light-driven Hydrogen Evolution. Angew. Chem. Int. Ed. *52,* 2435-2439.
5. Wang, H., Sun, Z., Li, Q., Tang, Q., and Wu, Z. (2016). Surprisingly Advanced CO_2 Photocatalytic Conversion over Thiourea Derived g-C_3N_4 with Water Vapor while Introducing 200–420 nm UV Light. J. CO_2 Util. *14*, 143-151.
6. Li, M., Zhang, L., Fan, X., Wu, M., Wang, M., Cheng, R., Zhang, L., Yao, H., and Shi, J. (2017). Core-shell $LaPO_4$/g-C_3N_4 Nanowires for Highly Active and Selective CO_2 Reduction. Appl. Catal. B-Environ. *201*, 629-635.
7. Li, M., Zhang, L., Wu, M., Du, Y., Fan, X., Wang, M., Zhang, L., Kong, Q., and Shi, J. (2016). Mesostructured CeO_2/g-C_3N_4 Nanocomposites: Remarkably Enhanced Photocatalytic Activity for CO_2 Reduction by Mutual Component Activations. Nano Energy *19*, 145-155.
8. Liu, B., Ye, L., Wang, R., Yang, J., Zhang, Y., Guan, R., Tian, L., and Chen, X. (2018). Phosphorus-Doped Graphitic Carbon Nitride Nanotubes with Amino-rich Surface for Efficient CO_2 Capture, Enhanced Photocatalytic Activity, and Product Selectivity. ACS Appl. Mater. Interfaces *10,* 4001-4009.
9. Fu, J., Zhu, B., Jiang, C., Cheng, B., You, W., and Yu, J. (2017). Hierarchical Porous O-Doped g-C_3N_4 with Enhanced Photocatalytic CO_2 Reduction Activity. Small *13,* 1603938.
10. Wang, M., Shen, M., Zhang, L., Tian, J., Jin, X., Zhou, Y., and Shi, J. (2017). 2D-2D MnO_2/g-C_3N_4 Heterojunction Photocatalyst: In-situ Synthesis and Enhanced CO_2Reduction Activity. Carbon *120,* 23-31.
11. Wang, J.C., Yao, H.C., Fan, Z.Y., Zhang, L., Wang, J.S., Zang, S.Q., and Li, Z.J. (2016). Indirect Z-Scheme BiOI/g-C_3N_4 Photocatalysts with Enhanced Photoreduction CO_2 Activity under Visible Light Irradiation. ACS Appl. Mater. Interfaces *8,* 3765-3775.
12. Li, M., Zhang, L., Fan, X., Zhou, Y., Wu, M., and Shi, J. (2015). Highly Selective CO_2 Photoreduction to CO over g-C_3N_4/Bi_2WO_6 Composites under Visible Light. J. Mater. Chem. A *3,* 5189-5196.
13. Di, T., Zhu, B., Cheng, B., Yu, J., and Xu, J. (2017). A Direct Z-scheme g-C_3N_4/SnS_2 Photocatalyst with Superior Visible-light CO_2 Reduction Performance. J. Catal. *352,* 532-541.
14. Yu, W., Xu, D., and Peng, T. (2015). Enhanced Photocatalytic Activity of g-C_3N_4 for Selective CO_2 Reduction to CH_3OH via Facile Coupling of ZnO: A Direct Z-scheme Mechanism. J. Mater. Chem. A *3,* 19936-19947.

15. Wang, Y., Bai, X., Qin, H., Wang, F., Li, Y., Li, X., Kang, S., Zuo, Y., and Cui, L. (2016). Facile One-Step Synthesis of Hybrid Graphitic Carbon Nitride and Carbon Composites as High-Performance Catalysts for CO_2 Photocatalytic Conversion. ACS Appl. Mater. Interfaces *8,* 17212-17219.
16. Ye, F., Wang, F., Meng, C., Bai, L., Li, J., Xing, P., Teng, B., Zhao, L., and Bai, S. (2018). Crystalline Phase Engineering on Cocatalysts: A Promising Approach to Enhancement on Photocatalytic Conversion of Carbon Dioxide to Fuels. Appl. Catal. B-Environ *230,* 145-153.
17. Shi, H., Chen, G., Zhang, C., and Zou, Z. (2014). Polymeric g-C_3N_4 Coupled with $NaNbO_3$ Nanowires toward Enhanced Photocatalytic Reduction of CO_2 into Renewable Fuel. ACS Catal. *4,* 3637-3643.
18. Zhou, H., Li, P., Liu, J., Chen, Z., Liu, L., Dontsova, D., Yan, R., Fan, T., Zhang, D., and Ye, J. (2016). Biomimetic Polymeric Semiconductor Based Hybrid Nanosystems for Artificial Photosynthesis towards Solar Fuels Generation via CO_2 Reduction. Nano Energy *25,* 128-135.
19. Tonda, S., Kumar, S., Bhardwaj, M., Yadav, P., and Ogale, S. (2018). g-C_3N_4/NiAl-LDH 2D/2D Hybrid Heterojunction for High-Performance Photocatalytic Reduction of CO_2 into Renewable Fuels. ACS Appl. Mater. Interfaces *10,* 2667-2678.
20. Li, P., Zhou, Y., Li, H., Xu, Q., Meng, X., Wang, X., Xiao, M., and Zou, Z. (2015). All-solid-state Z-scheme System Arrays of $Fe_2V_4O_{13}$/RGO/CdS for Visible Light-driving Photocatalytic CO_2 Reduction into Renewable Hydrocarbon Fuel. Chem. Commun. *51,* 800-803.
21. Cho, K.M., Kim, K.H., Park, K., Kim, C., Kim, S., Al-Saggaf, A., Gereige, I., and Jung, H.-T. (2017). Amine-Functionalized Graphene/CdS Composite for Photocatalytic Reduction of CO_2. ACS Catal. *7,* 7064-7069.
22. Shown, I., Hsu, H.C., Chang, Y.C., Lin, C.H., Roy, P.K., Ganguly, A., Wang, C.H., Chang, J.K., Wu, C.I., Chen, L.C., *et al.* (2014). Highly Efficient Visible Light Photocatalytic Reduction of CO_2 to Hydrocarbon Fuels by Cu-nanoparticle Decorated Graphene Oxide. Nano Lett. *14,* 6097-6103.
23. Yan, Y., Chen, J., Li, N., Tian, J., Li, K., Jiang, J., Liu, J., Tian, Q., and Chen, P. (2018). Systematic Bandgap Engineering of Graphene Quantum Dots and Applications for Photocatalytic Water Splitting and CO_2 Reduction. ACS Nano *12,* 3523-3532.
24. Yu, J., Jin, J., Cheng, B., and Jaroniec, M. (2014). A Noble Metal-free Reduced Graphene Oxide–CdS Nanorod Composite for the Enhanced Visible-light Photocatalytic Reduction of CO_2 to Solar Fuel. J. Mater. Chem. A *2,* 3407-3416.
25. Tu, W., Zhou, Y., Liu, Q., Tian, Z., Gao, J., Chen, X., Zhang, H., Liu, J., and Zou, Z. (2012). Robust Hollow Spheres Consisting of Alternating Titania Nanosheets and Graphene Nanosheets with High Photocatalytic Activity for CO_2 Conversion into Renewable Fuels. Adv. Funct. Mater. *22,* 1215-1221.
26. Xu, D., Cheng, B., Wang, W., Jiang, C., and Yu, J. (2018). Ag_2CrO_4/g-C_3N_4/graphene oxide Ternary Nanocomposite Z-scheme Photocatalyst with Enhanced CO_2 Reduction Activity. Appl. Catal. B-Environ. *231,* 368-380.

27. Wang, P.-Q., Bai, Y., Luo, P.-Y., and Liu, J.-Y. (2013). Graphene–WO_3 Nanobelt Composite: Elevated Conduction Band toward Photocatalytic Reduction of CO_2 into Hydrocarbon Fuels. Catal. Commun. *38*, 82-85.